

A cut finite element method for the Biot system of poroelasticity

Nanna Berre^{a,*}, Kent-Andre Mardal^{b,c}, André Massing^a, Ivan Yotov^d

^a*Department of Mathematical Sciences, Norwegian University of Science and Technology, Trondheim, Norway*

^b*Department of Numerical Analysis and Scientific Computing, Simula Research Laboratory, Oslo, Norway*

^c*Department of Mathematics, University of Oslo, Oslo, Norway*

^d*Department of Mathematics, University of Pittsburgh, Pittsburgh, USA*

Abstract

We propose a novel cut finite element method for the numerical solution of the Biot system of poroelasticity. The Biot system couples elastic deformation of a porous solid with viscous fluid flow and commonly arises on domains with complex geometries that make high-quality volumetric meshing challenging. To address this issue, we employ the cut finite element framework, where the domain boundary is represented independently of the background mesh, which significantly simplifies the meshing process. Our approach builds upon a parameter robust total pressure formulation of the Biot system, which we combine with the cut finite element method to develop a geometrically robust solution scheme, while preserving the parameter robustness. A key ingredient in the theoretical analysis is a modified inf-sup condition which also holds for mixed boundary conditions, leading to stability and optimal error estimates for the proposed formulation. Finally, we provide numerical evidence demonstrating the theoretical properties of the method and showcasing its capabilities by solving the Biot system on a realistic brain geometry.

Keywords: cut finite element methods, poroelasticity

1. Introduction

The Biot system [1] of poroelasticity models the flow of a viscous fluid in deformable porous media. It couples a momentum balance equation for the solid structure with a mass conservation equation for the fluid. The fluid pressure affects the solid stress, while the divergence of the solid displacement influences the fluid content, resulting in a fully coupled system. The numerical solution of the Biot system has been an active area of research, due to the numerous applications of the model in diverse fields, such as biomedicine, blood flow and organ tissue modeling, geosciences, groundwater flow, hydraulic fracturing, carbon sequestration, and landslides [2–10]. For the finite element-based numerical solution of the Biot system we refer the reader to two-field displacement–pressure formulations in [11, 12], three-field displacement–pressure–Darcy velocity formulations in [13–20], three-field displacement–pressure–total pressure formulations in [21, 22], four-field fully mixed stress–displacement–pressure–Darcy velocity formulations in [23], and five-field weakly symmetric stress–displacement–rotation–pressure–Darcy velocity formulations in [24, 25].

The above mentioned methods are based on finite element partitions that conform to the domain boundary. This may present challenges in applications with highly irregular geometries, e.g., brain or fracture networks, or time-dependent geometries, e.g., blood vessels, propagating fractures or sedimentary basins. Unfitted discretization methods such as the extended finite element method (XFEM) [26] are designed to remedy this issue by embedding the complex or changing geometry domain into a static domain with simple geometry partitioned by a regular grid. We refer to [27–31] for early work in this direction. A major challenge in unfitted methods is to ensure their geometrical robustness so that stability and accuracy are not compromised by small or arbitrarily cut elements. As a remedy, the cut finite element method (CutFEM) [32, 33] has emerged over the past 15 years as a powerful, general finite

*Corresponding author

Email addresses: nanna.berre@ntnu.no (Nanna Berre), kent-and@simula.no (Kent-Andre Mardal), andre.massing@ntnu.no (André Massing), yotov@math.pitt.edu (Ivan Yotov)

element methodology that provides a unified stabilization framework for the analysis of unfitted methods. Similar to the XFEM approach, boundary and interface conditions are weakly imposed using Nitsche’s method [34, 35, 35] or the Lagrange multiplier method [36]. In addition, so-called ghost penalty stabilization are incorporated into the discrete formulation which makes the resulting CutFEM scheme amendable to a geometrically robust stability and error analysis. Alternatively, strongly incorporated stabilization can be employed through the redefinition of the finite element spaces using aggregation techniques [37, 38]. As a result, a wide range of problem classes has been treated including, e.g., elliptic interface problems [39–41], Stokes and Navier-Stokes type problems [42–51], and complex multiphysic interface problems [52–56]. As a natural application area, unfitted finite element methods have also been proposed for problems in porous media [57–59], possibly including discrete fracture networks [30, 60–64]. We refer to [33, 65] and references therein for a comprehensive list of applications. An alternative approach is the shifted boundary method [66], which applies modified boundary conditions on a surrogate boundary consisting of faces of elements in the background mesh.

In this paper we employ the CutFEM methodology for the solution of the Biot system of poroelasticity, an approach that has so far received relatively little attention in the literature. CutFEM for the Biot consolidation model in a two-field displacement–pressure formulation has been studied in [67, 68]. In [67], the method is applied for modeling sedimentary basins with moving domains. The focus is on developing a fixed-stress iterative coupling method and the analysis of the convergence of the iteration. In [68], CutFEM is applied to the coupled Biot system. Extensive numerical studies are presented, but the theoretical stability and convergence of the method are not addressed. A CutFEM-based approach for coupling of incompressible fluid flow with poroelasticity is developed in [69], where numerical analysis is not presented.

1.1. Novel contributions and outline of the paper

The goal of this paper is to develop and analyse an unfitted CutFEM-based formulation for the Biot system of poroelasticity using a three-field displacement–pressure–total pressure formulation [21, 22]. The total pressure formulation has gained significant popularity due to its robustness with respect to the physical parameters. In particular, it avoids locking when the Lamé parameter $\lambda \rightarrow \infty$ and pressure oscillations when the permeability $K \rightarrow 0$. Our method is designed to carry over this parameter robustness to the cut finite element setting, while ensuring robustness with respect to the size of the cut elements. The latter is achieved by utilizing suitably scaled ghost penalty stabilization. We allow for both essential and natural boundary conditions for the displacement and the fluid pressure, with the essential boundary conditions being weakly enforced using Nitsche’s method.

We develop stability and error analysis of the proposed method. The norm of the fluid pressure has terms that are scaled by either K or λ^{-1} and we keep track of the dependence of the bounds on these parameters. As the finite elements for the displacement and total pressure form a Stokes-stable pair, we employ and extend previous results on CutFEM for the Stokes equations [42, 49, 70]. A key component in the stability analysis is establishing an inf-sup condition over the entire physical domain. The analysis in [49] assumes Dirichlet boundary conditions for the displacement everywhere and thus a zero mean value of the pressure. However, zero mean value for the total pressure cannot be assumed in the presented Biot discretization, as we need to consider both a perturbed saddle point problem as well as mixed boundary conditions. To deal with this issue, we combine the approach in [49] with an argument from [43, 70], to obtain a modified displacement–total pressure inf-sup condition containing a pressure ghost penalty as defect term. This approach necessitates the construction of a special interpolant with certain orthogonality property on the physical boundary, which is done by a patch-wise argument, extending the construction from [71]. As a result, we are able to establish stability and optimal-order error estimates for the method with constants independent of the size of the cut elements. We present extensive numerical results in two and three dimensions verifying the stability and convergence properties of the method and its robustness with respect to the physical parameters and how the physical domain cuts the background mesh. Furthermore, we present an example of using the method to model the flow in and deformation of the brain, which illustrates its robustness for complex physical applications with highly irregular three dimensional geometry and parameters in the locking regime.

The paper is structured as follows. In Section 2 we introduce the Biot system and briefly motivate the total pressure formulation, followed by the presentation of the proposed CutFEM formulation in Section 3. Afterwards, we collect necessary inequalities, interpolation results and present a detailed construction of the modified interpolant together with a brief discussion of ghost penalty realizations in Section 4. The main theoretical results including stability,

inf-sup conditions, and the final a priori error estimate are derived in Section 5. Finally, extensive numerical results are given in Section 6, before we draw our conclusions in Section 7.

2. Model problem

The quasi-static two field Biot's equations for a poroelastic material read

$$\begin{aligned} -\mu \nabla \cdot \varepsilon(\mathbf{u}) - \lambda \nabla \nabla \cdot \mathbf{u} + \alpha \nabla p_F &= \mathbf{f}, \\ \alpha \frac{\partial}{\partial t} \nabla \cdot \mathbf{u} + c_0 \frac{\partial}{\partial t} p_F - K \Delta p_F &= g, \end{aligned}$$

with the fundamental unknowns being the solid displacement \mathbf{u} and the fluid pressure p_F . A main challenge with Biot's equations is the large number of parameters (here assumed constant throughout the domain) μ , λ , α , c_0 and K , denoting the two Lamé parameters, the Biot-Willis constant, the constrained specific storage coefficient, and the hydraulic conductivity, respectively. In particular, locking may appear if $\lambda \gg \mu$ and pressure oscillations may appear as $K \rightarrow 0$.

To simplify the notation in the following we focus only on the parameters that cause numerical challenges. That is, let us consider $\alpha = 1$, $c_0 = 1/\lambda$ and a backward Euler time-discretization with $\Delta t = 1$. Then the above system reduces to

$$\begin{aligned} -\mu \nabla \cdot \varepsilon(\mathbf{u}) - \lambda \nabla \nabla \cdot \mathbf{u} + \nabla p_F &= \mathbf{f}, \\ -\nabla \cdot \mathbf{u} - \frac{1}{\lambda} p_F + K \Delta p_F &= g. \end{aligned}$$

Here, the sign is flipped on the second equation to obtain symmetry and g is altered to accommodate the sign change and source terms resulting from the time-discretization.

To briefly motivate the total pressure formulation, consider the Hermann trick of introducing a solid pressure $p_S = -\lambda \nabla \cdot \mathbf{u}$. Introducing the solid pressure, we arrive at

$$\begin{aligned} -\mu \nabla \cdot \varepsilon(\mathbf{u}) + \nabla p_S + \nabla p_F &= \mathbf{f}, \\ -\nabla \cdot \mathbf{u} - \frac{1}{\lambda} p_S &= 0, \\ -\nabla \cdot \mathbf{u} - \frac{1}{\lambda} p_F + K \Delta p_F &= g. \end{aligned}$$

In the case $K \rightarrow 0$ and $\lambda \rightarrow \infty$ we have two pressures to be determined by $\nabla \cdot \mathbf{u}$ and as such the system is degenerate. In the total pressure formulation an alternative pressure is introduced, namely $p_T = p_F + p_S$. The system then becomes

$$-\mu \nabla \cdot \varepsilon(\mathbf{u}) + \nabla p_T = \mathbf{f}, \tag{2.1}$$

$$-\nabla \cdot \mathbf{u} - \frac{1}{\lambda} p_T + \frac{1}{\lambda} p_F = 0, \tag{2.2}$$

$$\frac{1}{\lambda} p_T - \frac{2}{\lambda} p_F + K \Delta p_F = g. \tag{2.3}$$

Here, the degeneracy is eliminated at least on the continuous level, although, numerical issues may be present for certain schemes as $K \rightarrow 0$ and/or $\lambda \rightarrow \infty$. We remark that the total pressure formulation [21, 22] is just one of many formulations with the advantage that regular inf-sup stable Stokes elements can be used. We also note that as for Stokes problem, the case of pure Dirichlet conditions results in an undetermined constant for the pressure if $\lambda = \infty$. For λ large but not infinity the consequence is one bad mode. Such considerations are dealt with in detail in [21] and we will not focus on this case in the following.

The system (2.1)–(2.3) is supplemented with appropriate boundary conditions which we in accordance with [21] take to be

$$\mathbf{u} = \mathbf{u}_D \quad \text{on } \Gamma_d, \quad (2.4)$$

$$K \frac{\partial p_F}{\partial n} = g_N \quad \text{on } \Gamma_d, \quad (2.5)$$

$$(\mu \boldsymbol{\varepsilon}(\mathbf{u}) - p_T \mathbf{I}) \cdot \mathbf{n} = \boldsymbol{\sigma}_N \quad \text{on } \Gamma_s, \quad (2.6)$$

$$p_F = p_{F,D} \quad \text{on } \Gamma_s, \quad (2.7)$$

and we assume that Γ is of class C^2 . Throughout the remaining paper, we will make use of the following notation. The expression $a \lesssim (\gtrsim) b$ means that there exists a constant $C > 0$ independent of K , λ , and the mesh size h such that $a \leq (\geq) C b$. We write $a \sim b$ if $a \lesssim b \lesssim a$. Moreover, boldface symbols are used to denote vector valued functions or spaces. For inner products and norms on the Lebesgue space $L^2(\Omega)$ we use the notation $(\cdot, \cdot)_\Omega$ and $\|\cdot\|_\Omega$, respectively. We denote by $H^m(\Omega)$ the Sobolev space with weak derivatives up to order m in $L^2(\Omega)$ equipped with norm $\|\cdot\|_{m,\Omega}$. In addition, we use the following notation for an $H^m(\Omega)$ space with vanishing trace on a part of the boundary $\Gamma_X \subset \partial\Omega$:

$$H_{\Gamma_X,0}^m(\Omega) = \{p \in H^m(\Omega) \mid p|_{\Gamma_X} = 0\}.$$

A norm which involves a collection of geometric entities \mathcal{P}_h , should be understood a broken norm defined by $\|\cdot\|_{\mathcal{P}_h}^2 = \sum_{P \in \mathcal{P}_h} \|\cdot\|_P^2$, and similarly for inner products $(\cdot, \cdot)_{\mathcal{P}_h}$. Also, set operations involving \mathcal{P}_h should be understood as element-wise operations, e.g., $\mathcal{P}_h \cap U = \{P \cap U \mid P \in \mathcal{P}_h\}$, such that for inner products we have $(\cdot, \cdot)_{\mathcal{P}_h \cap U} = \sum_{P \in \mathcal{P}_h} (\cdot, \cdot)_{P \cap U}$. We define the trace space $H^{1/2}(\partial\Omega) = H^1(\Omega)|_{\partial\Omega}$, with norm $\|v\|_{H^{1/2}(\partial\Omega)} = \inf_{w \in H^1(\Omega), w|_{\partial\Omega} = v} \|w\|_{H^1(\Omega)}$, and correspondingly the trace space on part of the boundary, $H^{1/2}(\Gamma_X) = \{v|_{\Gamma_X} : v \in H^{1/2}(\partial\Omega)\}$, with norm $\|v\|_{H^{1/2}(\Gamma_X)} = \inf_{w \in H^1(\Omega), w|_{\Gamma_X} = v} \|w\|_{H^1(\Omega)}$, and $\widetilde{H}^{-1/2}(\Gamma_X) = [H^{1/2}(\Gamma_X)]^*$ as its dual space. We assume that $\mathbf{u}_D \in [H^{1/2}(\Gamma_d)]^n$, $p_D \in H^{1/2}(\Gamma_s)$, $\boldsymbol{\sigma}_N \in [\widetilde{H}^{-1/2}(\Gamma_s)]^n$, and $g_N \in \widetilde{H}^{-1/2}(\Gamma_d)$. For simplicity, we denote the dual pairing between $\widetilde{H}^{-1/2}(\Gamma_X)$ and $H^{1/2}(\Gamma_X)$ by $(\cdot, \cdot)_{\Gamma_X}$.

3. A cut finite element method for Biot's consolidation model

We let $\widetilde{\mathcal{T}}_h$ be a quasi uniform background mesh, consisting of shape regular closed simplices T covering $\overline{\Omega}$, see Figure 3.1. We denote the interior of the physical domain by $\Omega^\circ = \Omega \setminus \Gamma$. The *active mesh* \mathcal{T}_h is then defined as the collection of elements which intersect Ω ,

$$\mathcal{T}_h = \{T \in \widetilde{\mathcal{T}}_h \mid T \cap \Omega^\circ \neq \emptyset\},$$

which we further decompose into

$$\mathcal{T}_h^\Gamma = \{T \in \mathcal{T}_h \mid T \cap \Gamma \neq \emptyset\}, \quad \mathcal{T}_h^{\Gamma_s} = \{T \in \mathcal{T}_h \mid T \cap \Gamma_s \neq \emptyset\}, \quad \mathcal{T}_h^i = \mathcal{T}_h \setminus \mathcal{T}_h^\Gamma.$$

The set of interior facets associated with \mathcal{T}_h is denoted by

$$\mathcal{F}_h^i = \{F = T^+ \cap T^- \mid T^+, T^- \in \mathcal{T}_h \text{ and } 0 < |F|_{n-1} < \infty\}.$$

Here, $|F|_{n-1}$ is the $n - 1$ -dimensional Hausdorff measure of the facet F . We also introduce $\Omega_{\mathcal{T}} = \bigcup_{T \in \mathcal{T}_h} T$ as the domain covered by the active mesh.

For simplicity and following [21], we start from stable Stokes elements to discretize displacement and total pressure, more specifically (possibly higher order) Taylor-Hood elements. Alongside our presentation we will also briefly comment on possible extensions of the proposed cut finite element method to other inf-sup stable elements in the spirit of [49] and the use of strong stabilizations [38]. On the active mesh, we define discrete base function space to be

$$X_h^k := \mathbb{P}_c^k(\mathcal{T}_h) = \mathbb{P}^k(\mathcal{T}_h) \cap C^0(\mathcal{T}_h), \quad \text{where} \quad \mathbb{P}^k(\mathcal{T}_h) := \bigoplus_{T \in \mathcal{T}_h} \mathbb{P}^k(T),$$

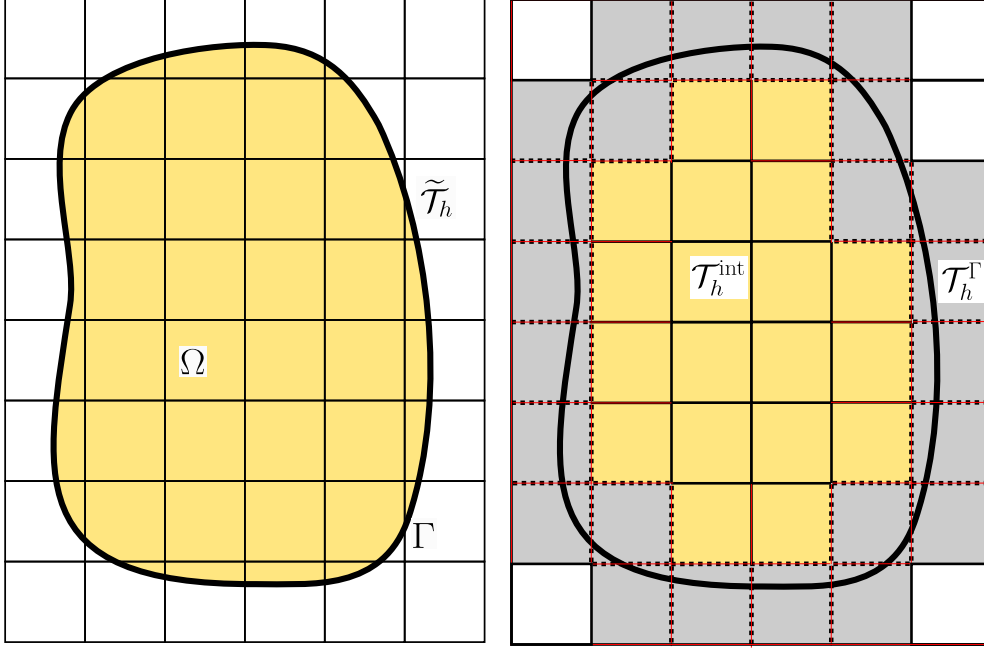


Figure 3.1: Example of an unfitted mesh, with the domain Ω inside the boundary Γ .

where $\mathbb{P}^k(T)$ denotes the set of all polynomials up to order k defined on T . Then, for $k \geq 2$, $l \geq 1$, the discrete function spaces for the displacement, fluid pressure, and total pressure are defined as

$$\mathbf{V}_h = [X_h^k]^n, \quad Q_{T,h} = X_h^{k-1}, \quad Q_{F,h} = X_h^l.$$

Note that the function spaces are now defined on the entire active mesh, instead of just the physical domain.

To derive a cut finite element method for Biot's equations, we first need to derive a preliminary formulation where all the relevant boundary conditions are enforced weakly. In this case we do not need to distinguish between discrete trial and test function spaces. Note that (2.6) and (2.5) are Neumann conditions for the displacement and fluid pressure, respectively, and thus will be naturally enforced weakly in the discrete formulation of (2.1) and (2.3), respectively. The Dirichlet conditions (2.4) and (2.7) on the other hand are typically strongly enforced in the continuous formulation, and thus will be now enforced weakly in the discrete formulation using Nitsche's method [34].

Starting from (2.1), we multiply by a discrete test function $\mathbf{v} \in \mathbf{V}_h$ and integrate by parts over Ω , incorporating (2.6) naturally on Γ_s and using Nitsche's method on Γ_d to incorporate (2.4) to see that, $\forall \mathbf{v}_h \in \mathbf{V}_h$,

$$\begin{aligned} & (\mu \boldsymbol{\varepsilon}(\mathbf{u}_h), \boldsymbol{\varepsilon}(\mathbf{v}_h))_\Omega - (\mu \boldsymbol{\varepsilon}(\mathbf{u}_h) \cdot \mathbf{n}, \mathbf{v}_h)_{\Gamma_d} - (\mathbf{u}_h, \mu \boldsymbol{\varepsilon}(\mathbf{v}_h) \cdot \mathbf{n})_{\Gamma_d} + \frac{\gamma_u}{h} \mu (\mathbf{u}_h, \mathbf{v}_h)_{\Gamma_d} - (p_{T,h}, \nabla \cdot \mathbf{v}_h)_\Omega \\ & + (p_{T,h}, \mathbf{v}_h \cdot \mathbf{n})_{\Gamma_d} = (\mathbf{f}, \mathbf{v}_h)_\Omega + (\boldsymbol{\sigma}_N, \mathbf{v}_h)_{\Gamma_s} - (\mathbf{u}_D, \mu \boldsymbol{\varepsilon}(\mathbf{v}_h) \cdot \mathbf{n})_{\Gamma_d} + \frac{\gamma_u}{h} \mu (\mathbf{u}_D, \mathbf{v}_h)_{\Gamma_d}. \end{aligned}$$

Turning to (2.2), we multiply by a discrete test function $q_{T,h} \in Q_{T,h}$ and add the consistent term $(\mathbf{u}_h - \mathbf{u}_D, q_{T,h} \mathbf{n})_{\Gamma_d}$ for symmetry reasons, leading to, $\forall q_{T,h} \in Q_{T,h}$,

$$-(\nabla \cdot \mathbf{u}_h, q_{T,h})_\Omega + (\mathbf{u}_h \cdot \mathbf{n}, q_{T,h})_{\Gamma_d} - \frac{1}{\lambda} (p_{T,h}, q_{T,h})_\Omega + \frac{1}{\lambda} (p_{F,h}, q_{T,h})_\Omega = (\mathbf{u}_D \cdot \mathbf{n}, q_{T,h})_{\Gamma_d}.$$

Finally, for (2.3) we multiply by a discrete test function $q_{F,h} \in Q_{F,h}$ and integrate by parts over Ω . This time, we

incorporate (2.5) naturally on Γ_d , while (2.7) is enforced weakly using Nitsche's method, obtaining, $\forall q_{F,h} \in Q_{F,h}$,

$$\begin{aligned} & \frac{1}{\lambda}(p_{T,h}, q_{F,h})_{\Omega} - \frac{2}{\lambda}(p_{F,h}, q_{F,h})_{\Omega} - (K\nabla p_{F,h}, \nabla q_{F,h})_{\Omega} \\ & \quad + (K\nabla p_{F,h} \cdot \mathbf{n}, q_{F,h})_{\Gamma_s} + (p_{F,h}, K\nabla q_{F,h} \cdot \mathbf{n})_{\Gamma_s} - \frac{\gamma_p}{h} K(p_{F,h}, q_{F,h})_{\Gamma_s} \\ & = (g, q_{F,h})_{\Omega} - (g_N, q_{F,h})_{\Gamma_d} + (p_{F,D}, K\nabla q_{F,h} \cdot \mathbf{n})_{\Gamma_s} - \frac{\gamma_p}{h} K(p_{F,D}, q_{F,h})_{\Gamma_s}. \end{aligned}$$

Next, set

$$\begin{aligned} a_{1,h}(\mathbf{u}_h, \mathbf{v}_h) &= (\mu \varepsilon(\mathbf{u}_h), \varepsilon(\mathbf{v}_h))_{\Omega} - (\mu \varepsilon(\mathbf{u}_h) \cdot \mathbf{n}, \mathbf{v}_h)_{\Gamma_d} - (\mathbf{u}_h, \mu \varepsilon(\mathbf{v}_h) \cdot \mathbf{n})_{\Gamma_d} + \frac{\gamma_u}{h} \mu(\mathbf{u}_h, \mathbf{v}_h)_{\Gamma_d}, \\ b_{1,h}(\mathbf{v}_h, p_{T,h}) &= -(\nabla \cdot \mathbf{v}_h, p_{T,h})_{\Omega} + (\mathbf{v}_h \cdot \mathbf{n}, p_{T,h})_{\Gamma_d}, \\ b_{2,h}(p_{F,h}, q_{T,h}) &= \frac{1}{\lambda}(p_{F,h}, q_{T,h})_{\Omega}, \\ a_{2,h}(p_{T,h}, q_{T,h}) &= \frac{1}{\lambda}(p_{T,h}, q_{T,h})_{\Omega}, \\ a_{3,h}^1(p_{F,h}, q_{F,h}) &= (K\nabla p_{F,h}, \nabla q_{F,h})_{\Omega} - (K\nabla p_{F,h} \cdot \mathbf{n}, q_{F,h})_{\Gamma_s} - (p_{F,h}, K\nabla q_{F,h} \cdot \mathbf{n})_{\Gamma_s} + \frac{\gamma_p}{h} K(p_{F,h}, q_{F,h})_{\Gamma_s}, \\ a_{3,h}^2(p_{F,h}, q_{F,h}) &= \frac{2}{\lambda}(p_{F,h}, q_{F,h})_{\Omega}, \\ a_{3,h}(p_{F,h}, q_{F,h}) &= a_{3,h}^1(p_{F,h}, q_{F,h}) + a_{3,h}^2(p_{F,h}, q_{F,h}) \\ L_1(\mathbf{v}_h) &= (\mathbf{f}, \mathbf{v}_h)_{\Omega} + (\sigma_N, \mathbf{v}_h)_{\Gamma_s} - (\mathbf{u}_D, \mu \varepsilon(\mathbf{v}_h) \cdot \mathbf{n})_{\Gamma_d} + \frac{\gamma_u}{h} \mu(\mathbf{u}_D, \mathbf{v}_h)_{\Gamma_d}, \\ L_2(q_{T,h}) &= (\mathbf{u}_D \cdot \mathbf{n}, q_{T,h})_{\Gamma_d}, \\ L_3(q_{F,h}) &= (g, q_{F,h})_{\Omega} - (g_N, q_{F,h})_{\Gamma_d} + (p_{F,D}, K\nabla q_{F,h} \cdot \mathbf{n})_{\Gamma_s} - \frac{\gamma_p}{h} K(p_{F,D}, q_{F,h})_{\Gamma_s}. \end{aligned}$$

Then a preliminary discrete weak formulation of Biot's equations is to find $(\mathbf{u}_h, p_{T,h}, p_{F,h}) \in \mathbf{V}_h \times Q_{T,h} \times Q_{F,h}$ such that

$$a_{1,h}(\mathbf{u}_h, \mathbf{v}_h) + b_{1,h}(\mathbf{v}_h, p_{T,h}) = L_1(\mathbf{v}_h), \quad \forall \mathbf{v}_h \in \mathbf{V}_h, \quad (3.1a)$$

$$b_{1,h}(\mathbf{u}_h, q_{T,h}) - a_{2,h}(p_{T,h}, q_{T,h}) + b_{2,h}(p_{F,h}, q_{T,h}) = L_2(q_{T,h}), \quad \forall q_{T,h} \in Q_{T,h}, \quad (3.1b)$$

$$b_{2,h}(q_{F,h}, p_{T,h}) - a_{3,h}(p_{F,h}, q_{F,h}) = L_3(q_{F,h}), \quad \forall q_{F,h} \in Q_{F,h}. \quad (3.1c)$$

We define the bilinear form B_h

$$\begin{aligned} B_h((\mathbf{u}_h, p_{T,h}, p_{F,h}), (\mathbf{v}_h, q_{T,h}, q_{F,h})) &= a_{1,h}(\mathbf{u}_h, \mathbf{v}_h) + b_{1,h}(\mathbf{v}_h, p_{T,h}) + b_{1,h}(\mathbf{u}_h, q_{T,h}) \\ & \quad - a_{2,h}(p_{T,h}, q_{T,h}) + b_{2,h}(p_{F,h}, q_{T,h}) + b_{2,h}(q_{F,h}, p_{T,h}) - a_{3,h}(p_{F,h}, q_{F,h}). \end{aligned} \quad (3.2)$$

We use the corresponding scaled discrete norms

$$\|\mathbf{v}_h\|_{\mathbf{V}_h}^2 = \mu \|\varepsilon(\mathbf{v}_h)\|_{\Omega}^2 + \gamma_u \mu \|h^{-1/2} \mathbf{v}_h\|_{\Gamma_d}^2, \quad (3.3)$$

$$\|q_{T,h}\|_{Q_{T,h}}^2 = \|q_{T,h}\|_{\Omega}^2, \quad (3.4)$$

$$\|q_{F,h}\|_{Q_{F,h}}^2 = K \|\nabla q_{F,h}\|_{\Omega}^2 + \gamma_p K \|h^{-1/2} q_{F,h}\|_{\Gamma_s}^2 + \lambda^{-1} \|q_{F,h}\|_{\Omega}^2. \quad (3.5)$$

In addition, we will also need the following norms

$$\|\mathbf{v}\|_{\mathbf{V}_{h,*}}^2 = \|\mathbf{v}\|_{\mathbf{V}_h}^2 + \mu \|h^{1/2} \mathbf{n} \cdot \nabla \mathbf{v}\|_{\Gamma_d}^2, \quad (3.6)$$

$$\|q_T\|_{Q_{T,*}}^2 = \|q_T\|_{Q_{T,h}}^2 + \|h^{1/2} q_T\|_{\Gamma_d}^2, \quad (3.7)$$

$$\|q_F\|_{Q_{F,h,*}}^2 = \|q_F\|_{Q_{F,h}}^2 + K \|h^{1/2} \mathbf{n} \cdot \nabla q_F\|_{\Gamma_s}^2, \quad (3.8)$$

$$\|(\mathbf{v}, q_T, q_F)\|_*^2 = \|\mathbf{v}\|_{\mathbf{V}_{h,*}}^2 + \|q_T\|_{Q_{T,*}}^2 + \|q_F\|_{Q_{F,h,*}}^2. \quad (3.9)$$

Remark 3.1. The functionals defined in (3.3) and (3.5) are indeed norms, using Korn's inequality [72, (1.19)] and Poincaré inequality [73, (1.10)].

The idea of the ghost penalty approach is to augment the formulation (3.1a)–(3.1c) above with certain stabilization forms $g_{1,h}(\cdot, \cdot)$, $g_{2,h}(\cdot, \cdot)$, and $g_{3,h}^i(\cdot, \cdot)$, $i = 1, 2$, acting the vicinity of the embedded boundary so that the norms above are extended to the entire active mesh \mathcal{T}_h , i.e.,

$$\begin{aligned}\|\mathbf{v}_h\|_{\mathbf{V}_h}^2 &= \|\mathbf{v}_h\|_{\mathbf{V}_h}^2 + |\mathbf{v}_h|_{g_{1,h}}^2 \sim \mu \|\varepsilon(\mathbf{v})\|_{\mathcal{T}_h}^2 + \gamma_u \mu \|h^{-1/2} \mathbf{v}\|_{\Gamma_d}^2, \\ \|q_{T,h}\|_{Q_{T,h}}^2 &= \|q_{T,h}\|_{Q_{T,h}}^2 + |q_{T,h}|_{g_{2,h}}^2 \sim \|q_{T,h}\|_{\mathcal{T}_h}^2, \\ \|q_{F,h}\|_{Q_{F,h}}^2 &= \|q_{F,h}\|_{Q_{F,h}}^2 + |q_{F,h}|_{g_{3,h}}^2 \sim \frac{1}{\lambda} \|q_{F,h}\|_{\mathcal{T}_h}^2 + K \|\nabla q_{F,h}\|_{\mathcal{T}_h}^2 + \gamma_p K \|h^{-1/2} q_{F,h}\|_{\Gamma_s}^2, \\ \|(\mathbf{v}_h, q_{T,h}, q_{F,h})\|_h^2 &= \|\mathbf{u}_h\|_{\mathbf{V}_h}^2 + \|p_{T,h}\|_{Q_{T,h}}^2 + \|p_{F,h}\|_{Q_{F,h}}^2.\end{aligned}$$

To this end, we replace the bilinear forms on the diagonal by their ghost-penalty enhanced counterparts

$$\begin{aligned}A_{1,h}(\mathbf{u}_h, \mathbf{v}_h) &= a_{1,h}(\mathbf{u}_h, \mathbf{v}_h) + g_{1,h}(\mathbf{u}_h, \mathbf{v}_h) \\ A_{2,h}(p_{T,h}, q_{T,h}) &= a_{2,h}(p_{T,h}, q_{T,h}) + g_{2,h}(p_{T,h}, q_{T,h}) \\ A_{3,h}^i(p_{F,h}, q_{F,h}) &= a_{3,h}^i(p_{F,h}, q_{F,h}) + g_{3,h}^i(p_{F,h}, q_{F,h}), \quad i = 1, 2,\end{aligned}$$

resulting in the ghost penalty cut finite element method: find $(\mathbf{u}_h, p_{T,h}, p_{F,h}) \in \mathbf{V}_h \times Q_{T,h} \times Q_{F,h}$ such that

$$\begin{aligned}A_{1,h}(\mathbf{u}_h, \mathbf{v}_h) + b_{1,h}(\mathbf{v}_h, p_{T,h}) &= L_1(\mathbf{v}_h), \quad \forall \mathbf{v}_h \in \mathbf{V}_h, \\ b_{1,h}(\mathbf{u}_h, q_{T,h}) - A_{2,h}(p_{T,h}, q_{T,h}) + b_{2,h}(p_{F,h}, q_{T,h}) &= L_2(q_{T,h}), \quad \forall q_{T,h} \in Q_{T,h}, \\ b_{2,h}(q_{F,h}, p_{T,h}) - A_{3,h}(p_{F,h}, q_{F,h}) &= L_3(q_{F,h}), \quad \forall q_{F,h} \in Q_{F,h}.\end{aligned}$$

Define the total ghost-penalty

$$G_h((\mathbf{u}_h, p_{T,h}, p_{F,h}), (\mathbf{v}_h, q_{T,h}, q_{F,h})) = g_{1,h}(\mathbf{u}_h, \mathbf{v}_h) + g_{2,h}(p_{T,h}, q_{T,h}) + g_{3,h}^1(p_{F,h}, q_{F,h}) + g_{3,h}^2(p_{F,h}, q_{F,h}),$$

and the total bilinear form

$$A_h((\mathbf{u}_h, p_{T,h}, p_{F,h}), (\mathbf{v}_h, q_{T,h}, q_{F,h})) = B_h((\mathbf{u}_h, p_{T,h}, p_{F,h}), (\mathbf{v}_h, q_{T,h}, q_{F,h})) + G_h((\mathbf{u}_h, p_{T,h}, p_{F,h}), (\mathbf{v}_h, q_{T,h}, q_{F,h})). \quad (3.11)$$

4. Useful inequalities, approximation properties and ghost penalty design

To prepare for the stability and error analysis in Section 5, we here collect some useful inequalities, discuss the construction and properties of various quasi-interpolation operators and review the design of suitable ghost penalties for the Biot problem.

4.1. Trace inequalities and inverse estimates

We recall the local trace inequalities, for a function $v \in H^1(T)$,

$$\|v\|_{\partial T} \lesssim h_T^{-1/2} \|v\|_T + h_T^{1/2} \|\nabla v\|_T, \quad \forall T \in \mathcal{T}_h, \quad (4.1)$$

$$\|v\|_{\Gamma \cap T} \lesssim h_T^{-1/2} \|v\|_T + h_T^{1/2} \|\nabla v\|_T, \quad \forall T \in \mathcal{T}_h. \quad (4.2)$$

In addition, we have the following inverse estimates for a discrete function $v_h \in \mathbb{P}^k(T)$ and $F \in \mathcal{F}_h(T) = \{F \in \mathcal{F}_h^i : |F \cap \partial T| > 0\}$

$$\|\nabla v_h\|_T \lesssim h_T^{-1} \|v_h\|_T, \quad (4.3)$$

$$\|\partial_n v_h\|_{F \cap \Omega} \lesssim h_T^{-1/2} \|v_h\|_T, \quad (4.4)$$

$$\|\partial_n v_h\|_{\Gamma \cap \Omega} \lesssim h_T^{-1/2} \|v_h\|_T. \quad (4.5)$$

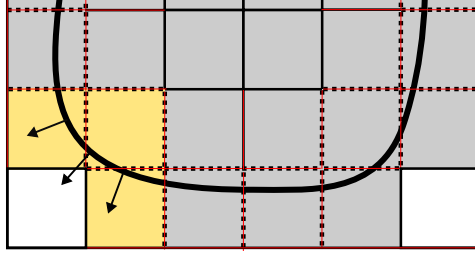


Figure 4.1: Example of a patch, with non-constant normal vector.

4.2. Quasi-interpolation operators

To obtain the required interpolation operator, we begin with the bounded extension operator $\mathcal{E} : H^s(\Omega) \rightarrow H^s(\mathbb{R}^n)$, $s \geq 0$, such that

$$\|\mathcal{E}u\|_{s,\mathbb{R}^n} \lesssim \|u\|_{s,\Omega},$$

see [74]. Next, define the polynomial space $V_h = X_h^k$ and let $\pi_h^* : L^2(\mathcal{T}_h) \rightarrow V_h$ be the standard Scott–Zhang interpolation which for $\forall T \in \mathcal{T}_h$ and $F \in \mathcal{F}_h(T)$ satisfies the interpolation error estimates

$$\begin{aligned} \|v - \pi_h^* v\|_{r,T} &\lesssim Ch^{s-r} |v|_{s,\mathcal{P}(T)}, & 0 \leq r \leq s \leq k+1, \\ \|v - \pi_h^* v\|_{r,F} &\lesssim Ch^{s-r-1/2} |v|_{s,\mathcal{P}(T)}, & 0 \leq r + \frac{1}{2} \leq s \leq k+1, \end{aligned}$$

where $\mathcal{P}(T)$ is the patch of neighbors of element T , meaning the domain including all elements sharing at least one vertex with T . Further, we define $\pi_h : L^2(\Omega) \rightarrow V_h$ as follows:

$$\pi_h v = \pi_h^* \mathcal{E}v. \quad (4.6)$$

The stability of the extension operator \mathcal{E} together with the interpolation error for the Scott–Zhang operator imply the following interpolation estimates:

$$\|\mathcal{E}v - \pi_h v\|_{r,\mathcal{T}_h} \lesssim Ch^{s-r} |v|_{s,\Omega}, \quad 0 \leq r \leq s \leq k+1, \quad (4.7)$$

$$\|\mathcal{E}v - \pi_h v\|_{r,\mathcal{F}_h} \lesssim Ch^{s-r-1/2} |v|_{s,\Omega}, \quad 0 \leq r + \frac{1}{2} \leq s \leq k+1. \quad (4.8)$$

For the norms (3.6)–(3.8), this then gives following the interpolation estimates.

Lemma 4.1 (Interpolation estimates). *Assume $v \in [H^r(\Omega)]^n$, $q_T \in H^s(\Omega)$, $q_F \in H^s(\Omega)$, and let $\pi_h v \in [X_h^k]^n$, $\pi_h q_T \in X_h^m$, $\pi_h q_F \in X_h^l$. Then for $\bar{r} = \min\{k+1, r\}$, $\bar{s} = \min\{m+1, s\}$, and $\bar{t} = \min\{l+1, t\}$ we have the following estimates*

$$\begin{aligned} \|v - \pi_h v\|_{V_{h,*}} &\lesssim \mu^{1/2} h^{\bar{r}-1} |v|_{\bar{r}}, \\ \|q_T - \pi_h q_T\|_{Q_{T,h,*}} &\lesssim h^{\bar{s}} |q_T|_{\bar{s}}, \\ \|q_F - \pi_h q_F\|_{Q_{F,h,*}} &\lesssim (K^{1/2} + \lambda^{-1/2} h) h^{\bar{t}-1} |q_F|_{\bar{t}}. \end{aligned}$$

We need the interpolant to have additional orthogonality properties on the interface, which we get from a modified Scott–Zhang operator introduced in [71]. To construct this interpolant, we first define the set of all elements that intersect the interface Γ_s and elements that share a face or vertex with these elements,

$$\overline{\mathcal{T}}_h^{\Gamma_s} = \{T \in \mathcal{T}_h \mid T \cap T' \neq \emptyset, T' \in \mathcal{T}_h^{\Gamma_s}\}.$$

Next, we regroup the elements in $\overline{\mathcal{T}}_h^{\Gamma_s}$ into non-overlapping patches $\{\mathcal{P}_i\}_{i=1}^N$ such that for each patch, a patch function ϕ_i can be constructed from the basis functions with support in \mathcal{P}_i . Further, \mathcal{P}_i and ϕ_i have the properties

1. $h \lesssim \text{diam}(\mathcal{P}_i) \lesssim h$,
2. $h^{n-1} \lesssim \int_{\Gamma_s \cap \mathcal{P}_i} \phi_i \lesssim h^{n-1}$,
3. $h^{-1} \lesssim |\nabla \phi_i(x)| \lesssim h^{-1}$.

In contrast to the proof given in [71], we allow for *non-constant* normal vectors on each patch, see Figure 4.1 for an example of such a patch. This is particularly important if we want to consider the use of independently generated surface meshes or higher-order implicit descriptions to represent the embedded surface. To take patch-wise normal-field variations into account, we recall that the boundary Γ_s is assumed to be of class C^2 , and we therefore know that there exists an ε -tubular neighborhood $U_\varepsilon(\Gamma_s)$, and an ε_0 such that there is a unique closest point $p(x)$ on Γ_s for all $x \in U_{\varepsilon_0}(\Gamma_s)$ where $|x - p(x)| = \text{dist}(\Gamma_s, x)$. Choosing h small enough, we have that $\overline{\mathcal{T}}_h^{\Gamma_s}$ is contained in $U_{\varepsilon_0}(\Gamma_s)$. Choosing $\mathbf{x}_0 \in \mathcal{P}_i \cap \Gamma_s$, the following bound holds for the normal vector

$$\|\mathbf{n}(\mathbf{x}) - \mathbf{n}(\mathbf{x}_0)\|_{\infty, \mathcal{P}_i \cap \Gamma_s} \leq \|\nabla \mathbf{n}\|_{\infty, \mathcal{P}_i} \|\mathbf{x} - \mathbf{x}_0\|_{\infty, \mathcal{P}_i \cap \Gamma_s} \leq c_I h, \quad (4.10)$$

so that c_I is the maximum of the principal curvatures.

We want the modified interpolant to satisfy the following orthogonality property

$$\int_{\mathcal{P}_i \cap \Gamma_s} (\mathbf{v} - \pi_h^c \mathbf{v}) \cdot \mathbf{n} \, ds = 0, \quad (4.11)$$

for all \mathcal{P}_i . In [71] the normal was implicitly assumed to be constant on each patch. In the following we will extend the construction to non-constant normal vectors, and dimension n .

Lemma 4.2. *There exists a modified Scott–Zhang interpolation operator $\pi_h^c : H^1(\Omega_h) \rightarrow V_h$ which for $\forall \mathbf{v} \in [H^r(\Omega)]^n$, $r \geq 1$ satisfies both the orthogonality property (4.11) and the interpolation estimate*

$$\|\mathbf{v} - \pi_h^c \mathbf{v}\|_{\mathcal{T}_h} + h \|\nabla (\mathbf{v} - \pi_h^c \mathbf{v})\|_{\mathcal{T}_h} \lesssim h \|\mathbf{v}\|_{1, \Omega}. \quad (4.12)$$

Proof. Let \mathbf{Y}_i be the (vector-valued) degree of freedom associated with ϕ_i defined on a patch \mathcal{P}_i . Let $\mathbf{e}^1(\mathbf{x}) = \mathbf{n}(\mathbf{x})$ the surface normal, and define $\mathbf{e}^k(\mathbf{x})$ for $k = 2, \dots, n$ to be orthogonal vectors such that they span the tangential space $T_x \Gamma_s$. We determine \mathbf{Y}_i from the linear system

$$\int_{\mathcal{P}_i \cap \Gamma_s} \mathbf{Y}_i \cdot \mathbf{e}^k \phi_i \, ds = \int_{\mathcal{P}_i \cap \Gamma_s} (\mathbf{v} - \pi_h \mathbf{v}) \cdot \mathbf{e}^k \, ds \quad \text{for } k = 1, \dots, n,$$

which we can write as the matrix equation

$$A_i \mathbf{Y}_i = \mathbf{V}_i,$$

with

$$A_i = \begin{bmatrix} \int_{\mathcal{P}_i \cap \Gamma_s} \phi_i (\mathbf{e}^1)^T \, ds \\ \vdots \\ \int_{\mathcal{P}_i \cap \Gamma_s} \phi_i (\mathbf{e}^n)^T \, ds \end{bmatrix}, \quad \mathbf{V}_i = \begin{bmatrix} \int_{\mathcal{P}_i \cap \Gamma_s} (\mathbf{v} - \pi_h \mathbf{v}) \cdot \mathbf{e}^1 \, ds \\ \vdots \\ \int_{\mathcal{P}_i \cap \Gamma_s} (\mathbf{v} - \pi_h \mathbf{v}) \cdot \mathbf{e}^n \, ds \end{bmatrix}.$$

Next, let $\bar{\mathbf{e}}_i^k = \mathbf{e}^k(\mathbf{x}_0)$ for an $\mathbf{x}_0 \in \mathcal{P}_i \cap \Gamma_s$, and define the matrix B_i

$$B_i = \int_{\mathcal{P}_i \cap \Gamma_s} \phi_i \, ds \begin{bmatrix} (\bar{\mathbf{e}}^1)^T \\ \vdots \\ (\bar{\mathbf{e}}^n)^T \end{bmatrix}.$$

From construction, B_i is an invertible matrix, the Euclidean based matrix norm can easily be estimated $|B_i|_{\mathbb{R}^n} \sim h^{n-1}$, and it follows that $|B_i^{-1}|_{\mathbb{R}^n} \lesssim h^{1-n}$. We also define the matrix C_i , with elements $C_i^{k,j} = \int_{\mathcal{P}_i \cap \Gamma_s} (\mathbf{e}^{k,j} - \bar{\mathbf{e}}_i^{k,j}) \phi \, ds$, where $\mathbf{e}^{k,j}$

is j -th component of \mathbf{e}^k . Recall the bound of the normal vector (4.10), which is also valid for the orthogonal vectors, so that for one element in C_i

$$|C_i^{k,j}| \leq \|e_i^{k,j} - \tilde{e}_i^{k,j}\|_{\infty, \mathcal{P}_i \cap \Gamma_s} \int_{\mathcal{P}_i \cap \Gamma_s} |\phi| \, ds \lesssim h^n,$$

giving $|C_i|_{\mathbb{R}^n} \lesssim h^n$. We can write $A_i = B_i + C_i = B_i(\mathcal{I} + B_i^{-1}C_i)$, and in addition we have

$$|B_i^{-1}C_i|_{\mathbb{R}^n} \leq |B_i^{-1}|_{\mathbb{R}^n} |C_i|_{\mathbb{R}^n} \lesssim h, \quad (4.13)$$

meaning that for small h , A_i is invertible and \mathbf{Y}_i is given by $\mathbf{Y}_i = A_i^{-1}\mathbf{V}_i$. We want to establish a bound for $|\mathbf{Y}_i|_{\mathbb{R}^n} \leq |A_i^{-1}|_{\mathbb{R}^n} |\mathbf{V}_i|_{\mathbb{R}^n}$, and begin by finding a bound for $|A_i^{-1}|_{\mathbb{R}^n}$,

$$|A_i^{-1}|_{\mathbb{R}^n} = |(\mathcal{I} + B_i^{-1}C_i)^{-1}B_i^{-1}|_{\mathbb{R}^n} \lesssim |(\mathcal{I} + B_i^{-1}C_i)^{-1}|_{\mathbb{R}^n} |B_i^{-1}|_{\mathbb{R}^n}.$$

For small h we can use power series expansion together with (4.13) to get

$$\begin{aligned} |A_i^{-1}|_{\mathbb{R}^n} &\leq |(\mathcal{I} + B_i^{-1}C_i)^{-1}|_{\mathbb{R}^n} |B_i^{-1}|_{\mathbb{R}^n} = \left| \sum_{k=0}^{\infty} (-B_i^{-1}C_i)^k \right|_{\mathbb{R}^n} |B_i^{-1}|_{\mathbb{R}^n} \\ &\leq \sum_{k=0}^{\infty} |B_i^{-1}C_i|_{\mathbb{R}^n}^k |B_i^{-1}|_{\mathbb{R}^n} = \frac{|B_i^{-1}|_{\mathbb{R}^n}}{1 - |B_i^{-1}C_i|_{\mathbb{R}^n}} \lesssim \frac{|B_i^{-1}|_{\mathbb{R}^n}}{1 - h} \lesssim h^{1-n}. \end{aligned} \quad (4.14)$$

Next, we apply a Cauchy-Schwarz inequality, the trace inequality (4.2), and the approximation properties of π_h to obtain

$$\begin{aligned} |\mathbf{V}_i^k| &= \left| \int_{\mathcal{P}_i \cap \Gamma_s} (\mathbf{v} - \pi_h \mathbf{v}) \mathbf{e}^k \, ds \right| \\ &\lesssim h^{(n-1)/2} \|\mathbf{v} - \pi_h \mathbf{v}\|_{\mathcal{P}_i \cap \Gamma_s} \\ &\lesssim h^{n/2-1} \|\mathbf{v} - \pi_h \mathbf{v}\|_{\mathcal{P}_i} + h^{n/2} \|\nabla(\mathbf{v} - \pi_h \mathbf{v})\|_{\mathcal{P}_i} \\ &\lesssim h^{n/2} \|\nabla \mathbf{v}\|_{\mathcal{P}(\mathcal{P}_i)}, \end{aligned}$$

where $\mathcal{P}(\mathcal{P}_i)$ consists of all the patches that share a vertex with \mathcal{P}_i . Then, combining this with (4.14) we get the following bound for \mathbf{Y}_i

$$|\mathbf{Y}_i|_{\mathbb{R}^n} \leq |A_i^{-1}|_{\mathbb{R}^n} |\mathbf{V}_i|_{\mathbb{R}^n} \leq Ch^{-n/2+1} \|\nabla \mathbf{v}\|_{\mathcal{P}(\mathcal{P}_i)}.$$

The modified interpolant is defined by

$$\pi_h^c \mathbf{v} = \pi_h \mathbf{v} + \sum_{i=1}^N \phi_i \mathbf{Y}_i. \quad (4.15)$$

Next, for a $K \in \mathcal{P}_i$ we have that

$$\begin{aligned} \|\mathbf{v} - \pi_h^c \mathbf{v}\|_K &\leq \|\mathbf{v} - \pi_h \mathbf{v}\|_K + \|\phi_i \mathbf{Y}_i\|_K \\ &\lesssim \|\mathbf{v} - \pi_h \mathbf{v}\|_K + h^{n/2} |\mathbf{Y}_i|_{\mathbb{R}^n} \\ &\lesssim \|\mathbf{v} - \pi_h \mathbf{v}\|_K + h \|\nabla \mathbf{v}\|_{\mathcal{P}(\mathcal{P}_i)}, \end{aligned}$$

and similarly,

$$\begin{aligned} \|\nabla(\pi_h^c \mathbf{v})\|_K &\leq \|\nabla(\pi_h \mathbf{v})\|_K + \|\nabla(\phi_i \mathbf{Y}_i)\|_K \\ &\lesssim \|\nabla(\pi_h \mathbf{v})\|_K + h^{n/2-1} |\mathbf{Y}_i|_{\mathbb{R}^n} \\ &\lesssim \|\nabla(\pi_h \mathbf{v})\|_K + \|\nabla \mathbf{v}\|_{\mathcal{P}(\mathcal{P}_i)}, \end{aligned} \quad (4.16)$$

which together with the properties of π_h , and that we by construction have a bounded number of patch overlaps leads to desired interpolation estimate

$$\|\mathbf{v} - \pi_h^c \mathbf{v}\|_{\mathcal{T}_h} + h \|\nabla(\mathbf{v} - \pi_h^c \mathbf{v})\|_{\mathcal{T}_h} \lesssim h \|\mathbf{v}\|_{1,\Omega}.$$

□

4.3. Role and design of ghost penalties

The total pressure formulation (3.10)–(3.11) can be seen as perturbed Stokes problem for the displacement and total pressure which is intertwined with a Poisson problem for the fluid pressure. Thus, to devise suitable ghost penalty stabilization, we have to take into account the different roles played by the individual bilinear form contributions. To do so, we start our discussion from an abstract finite element space \mathcal{V}_h satisfying $\mathbb{P}_c^k(\mathcal{T}_h) \subset \mathcal{V}_h$ and review the required properties for H^1 stabilizing ghost penalty $g_h(\cdot, \cdot)$ suitable for cut finite element formulations of elliptic problems, see e.g. [33, 41]. Then, departing from this abstract setting, we discuss the specific ghost penalties needed for the relevant bilinear forms appearing in (3.2).

4.3.1. H^1 -stabilizing ghost penalties and realizations

We assume that the ghost penalty $g_h(\cdot, \cdot)$ is a symmetric positive semi-definite bilinear form on \mathcal{V}_h satisfying the following assumptions:

A1 H^1 semi-norm extension property for $v_h \in \mathcal{V}_h$,

$$\|\nabla v_h\|_{\mathcal{T}_h} \lesssim \|\nabla v_h\|_{\Omega_h^i} + |v_h|_{g_h}, \quad (4.17)$$

A2 Weak consistency for $v \in H^s(\Omega)$,

$$|\pi_h v|_{g_h} \lesssim h^{r-1} \|v\|_{r, \Omega}, \quad (4.18)$$

where $r = \min\{s, k + 1\}$ and π_h is the quasi-interpolation operator given in (4.6).

These two properties are crucial for deriving geometrically robust discrete coercivity and optimal a priori error estimates for cut finite element formulation of Poisson-type problems, see [33, 41]. To ensure that the associated system matrices satisfy the usual condition number bounds, we typically require the following additional properties to be satisfied by the ghost penalty $g_h(\cdot, \cdot)$:

A3 L^2 norm extension property for $v_h \in \mathcal{V}_h$,

$$\|v_h\|_{\mathcal{T}_h} \lesssim \|v_h\|_{\Omega_h^i} + |v_h|_{g_h}. \quad (4.19)$$

A4 Inverse inequality for $v_h \in \mathcal{V}_h$,

$$|v_h|_{g_h} \lesssim h^{-1} \|v_h\|_{\mathcal{T}_h}. \quad (4.20)$$

Next, we briefly review the most common realizations of the ghost penalty $g_h(\cdot, \cdot)$ satisfying Assumptions 4.17–4.20 for \mathcal{V}_h . *Facet-based* ghost penalties [70, 71, 75]

$$g_h^f(v, w) = \sum_{j=0}^p \gamma_p^f h^{2j-1} (\llbracket \partial_n^j v \rrbracket, \llbracket \partial_n^j w \rrbracket)_{\mathcal{F}_h^g}, \quad (4.21)$$

penalizes the jumps of normal-derivatives of all relevant polynomial orders across faces belonging to the facet set

$$\mathcal{F}_h^g = \{F \in \mathcal{F}_h : T^+ \cap \Gamma \neq \emptyset \vee T^- \cap \Gamma \neq \emptyset\}.$$

Here, we use the notation $\partial_n^j v := \sum_{|\alpha|=j} \frac{D^\alpha v(x) n^\alpha}{\alpha!}$ for multi-indices $\alpha = (\alpha_1, \dots, \alpha_d)$, $|\alpha| = \sum_i \alpha_i$ and $n^\alpha = n_1^{\alpha_1} n_2^{\alpha_2} \dots n_d^{\alpha_d}$. The constant γ^f denotes a dimensionless stability parameter. Note that for H^1 -conforming finite element spaces, the jump terms for $j = 0$ vanish.

In [75], ghost penalties based on a *local projection stabilization* were proposed. For a given patch P of $\text{diam}(P) \lesssim h$ containing the two elements T_1 and T_2 , one defines the L^2 projection $\pi_P : L^2(P) \rightarrow \mathbb{P}_p(P)$ onto the space of polynomials of order p associated with the patch P . For $v \in V_h$, the fluctuation operator $\kappa_P = I - \pi_P$ measures then the deviation of $v|_P$ from being a polynomial defined on P . By choosing certain patch definitions, a coupling between

elements with a possible small cut and an interior element is ensured. One patch choice arises naturally from the definition of \mathcal{F}_h^g by defining the patch $P(F) = T_F^+ \cup T_F^-$ for two elements T_F^+, T_F^- sharing the interior face F and setting

$$\mathcal{P}_1 = \{P(F)\}_{F \in \mathcal{F}_h^g}.$$

A second possibility is to use neighborhood patches $\omega(T)$,

$$\mathcal{P}_2 = \{\omega(T)\}_{T \in \mathcal{T}_h^T}.$$

Alternatively, one can mimic the cell agglomeration approach taken in classical unfitted finite element methods approaches [37, 38, 76] by associating to each cut element $T \in \mathcal{T}_h^T$ with a small intersection $|T \cap \Omega|_d \ll |T|_d$ an element $T' \in \mathcal{T}_h^I$ such that the ‘‘agglomerated patch’’ $P_a(T) = T \cup T'$ satisfies $\text{diam } P_a(T) \lesssim h$. A proper collection of patches is then given by

$$\mathcal{P}_3 = \{P_a(T)\}_{T \in \mathcal{T}_h^T}.$$

The resulting *local projection* based ghost penalty are then defined as follows:

$$g_h^p(v, w) = \gamma^p \sum_{P \in \mathcal{P}} h^{-2} (\kappa_P v, \kappa_P w)_P, \quad \mathcal{P} \in \{\mathcal{P}_1, \mathcal{P}_2, \mathcal{P}_3\}.$$

Finally, an elegant version of a patch-based ghost penalty avoiding the use of local projection operators was presented in [77]. By extending polynomials u_i defined on an element T_i naturally to global polynomials u_i^e , a volume-based jump on a patch $P = T_1 \cup T_2$ can be defined by $\llbracket u \rrbracket_P = u_1^e - u_2^e$ which give rise to the *volume based* ghost penalty

$$g_h^v(v, w) = \gamma_b^v \sum_{P \in \mathcal{P}_1} h^{-2} (\llbracket v \rrbracket_P, \llbracket w \rrbracket_P)_P, \quad \mathcal{P} \in \{\mathcal{P}_1, \mathcal{P}_2, \mathcal{P}_3\}.$$

More realizations with alternative penalty operator and patch choices can be found in the literature, see e.g. [33] and the references therein.

4.3.2. Ghost penalties for the Biot problem

Starting from abstract setting, we define the individual ghost penalties for the relevant bilinear forms appearing in (3.2) as follows:

$$\begin{aligned} g_{1,h}(\mathbf{u}_h, \mathbf{v}_h) &= \mu g_h(\mathbf{u}_h, \mathbf{v}_h), & \forall \mathbf{u}_h, \mathbf{v}_h \in \mathbf{V}_h, \\ g_{2,h}(p_{T,h}, q_{T,h}) &= h^2 g_h(p_{T,h}, q_{T,h}), & \forall p_{T,h}, q_{T,h} \in Q_{T,h}, \\ g_{3,h}^1(p_{F,h}, q_{F,h}) &= K g_h(p_{F,h}, q_{F,h}), & \forall p_{F,h}, q_{F,h} \in Q_{F,h}, \\ g_{3,h}^2(p_{F,h}, q_{F,h}) &= \frac{1}{\lambda} g_h(p_{F,h}, q_{F,h}), & \forall p_{F,h}, q_{F,h} \in Q_{F,h}. \end{aligned}$$

Here, we have tacitly assumed that $g_h(\cdot, \cdot)$ can be defined analogously for vector-valued arguments $\mathbf{u}_h, \mathbf{v}_h \in \mathbf{V}_h$.

The scaling of the individual ghost penalties is chosen to match the scaling of the corresponding bilinear forms in (3.2). In particular, the h^2 -scaling appearing in $g_{2,h}(\cdot, \cdot)$ reflects the fact that the pressure $p_{T,h}$ needs to be controlled in an L^2 -like norm, and later we will see that the h -scaled H^1 semi-norm $\|h \nabla p_{T,h}\|_{\mathcal{T}_h}$ of the pressure naturally appears in the analysis of the discrete inf-sup condition, see Assumption 5.1. To prepare for this, we record here some important properties of the pressure ghost penalty $g_{2,h}(\cdot, \cdot)$ which follow directly from the assumptions for the abstract ghost penalty $g_h(\cdot, \cdot)$. First, using Assumption A1, we see that

$$\|h \nabla p_{T,h}\|_{\mathcal{T}_h} \lesssim \|h \nabla p_{T,h}\|_{\Omega_h^i} + |p_{T,h}|_{g_{2,h}} \lesssim \|p_{T,h}\|_{\mathcal{T}_h}, \quad \forall p_{T,h} \in Q_{T,h}, \quad (4.22)$$

where the second inequality follows from A4 and the usual inverse estimate (4.3). Second, using Assumption A2, we have the weak consistency estimate

$$|\pi_h p_T|_{g_{2,h}} \lesssim h^{\bar{s}} \|p_T\|_{\bar{s}, \Omega}, \quad \forall p_T \in H^s(\Omega),$$

where $\pi_h : L^2(\Omega) \rightarrow Q_{T,h}$ is the quasi-interpolation operator given in (4.6) with $V_h = X_h^l$ and $\bar{s} = \min\{s, l+1\}$.

5. Stability and a priori error analysis

This section is devoted to the theoretical analysis of the cut finite element method (3.10) for the Biot problem. We start by collecting the necessary stability and coercivity estimates for the bilinear forms involved, before we turn to the discussion of a modified inf-sup condition for the displacement-total-pressure coupling bilinear form $b_{1,h}(\cdot, \cdot)$ when mixed boundary conditions are considered. Afterwards, we state and prove the main inf-sup condition for total bilinear form $A_h(\cdot, \cdot)$ given in (3.11). Here, the main objectives are to carry over the parameter robustness of the total pressure formulation to the cut finite element setting, and to ensure that the resulting unfitted method is also geometrically robust. We conclude the section by deriving optimal a priori error estimates for the proposed cut finite element method.

5.1. Stability estimates

Lemma 5.1. *Assuming that γ_u and γ_p are sufficiently large, it holds that*

$$A_{1,h}(\mathbf{v}_h, \mathbf{v}_h) \geq c_{A_1} \|\mathbf{v}_h\|_{\mathbf{V}_h}^2, \quad \forall \mathbf{u}_h, \mathbf{v}_h \in \mathbf{V}_h, \quad (5.1)$$

$$A_{3,h}(q_{F,h}, q_{F,h}) \geq c_{A_3} \|q_{F,h}\|_{Q_{F,h}}^2, \quad \forall p_{F,h}, q_{F,h} \in Q_{F,h}, \quad (5.2)$$

$$A_{1,h}(\mathbf{u}_h, \mathbf{v}_h) \leq C_{A_1} \|\mathbf{u}_h\|_{\mathbf{V}_h} \|\mathbf{v}_h\|_{\mathbf{V}_h}, \quad \forall \mathbf{u}_h, \mathbf{v}_h \in \mathbf{V}_h \quad (5.3)$$

$$a_{1,h}(\mathbf{u}, \mathbf{v}_h) \lesssim \|\mathbf{u}\|_{\mathbf{V}_{h,*}} \|\mathbf{v}_h\|_{\mathbf{V}_h}, \quad \forall (\mathbf{u}, \mathbf{v}_h) \in [H^2(\Omega)]^n \times \mathbf{V}_h, \quad (5.4)$$

$$a_{2,h}(q_T, q_{T,h}) \lesssim \lambda^{-1} \|q_T\|_{Q_{T,h}} \|q_{T,h}\|_{Q_{T,h}}, \quad \forall (q_T, q_{T,h}) \in H^1(\Omega) \times Q_{T,h}, \quad (5.5)$$

$$a_{3,h}(q_F, q_{F,h}) \lesssim \|q_F\|_{Q_{F,h,*}} \|q_{F,h}\|_{Q_{F,h}}, \quad \forall (q_F, q_{F,h}) \in H^2(\Omega) \times Q_{F,h}, \quad (5.6)$$

$$b_{1,h}(\mathbf{v}, q_T) \lesssim \|\mathbf{v}\|_{\mathbf{V}_{h,*}} \|q_T\|_{Q_{T,h,*}}, \quad \forall (\mathbf{v}, q_T) \in [H^1(\Omega)]^n \times H^1(\Omega), \quad (5.7)$$

$$b_{2,h}(q_T, q_F) \lesssim \lambda^{-1} \|q_T\|_{L^2(\Omega)} \|q_F\|_{Q_{F,h}}, \quad \forall (q_T, q_F) \in H^1(\Omega) \times H^1(\Omega). \quad (5.8)$$

Proof. We recognize the bilinear form $a_{3,h}$ from an elliptic problem, and $a_{1,h}$, $a_{2,h}$ and $b_{1,h}$ from the Stokes problem, and similarly with the stabilized forms. Proof of coercivity and boundedness follows from the standard arguments for these bilinear forms, see e.g. [35, 46, 70, 75]. \square

Next, we recall the assumption from [49], where we will make use of the function space $H_0^1(\mathcal{T}_h^i) = \{v \in H^1(\mathcal{T}_h^i) : v = 0 \text{ on } \partial\mathcal{T}_h^i\}$.

Assumption 5.1. [49] *Assume there exists $\beta > 0$ independent of h , depending only on polynomial degree of finite element spaces and the shape regularity of \mathcal{T}_h such that*

$$\beta \|h \nabla q\|_{\mathcal{T}_h^i} \leq \sup_{\mathbf{v} \in \mathbf{V}_h^i} \frac{(\nabla \cdot \mathbf{v}, q)_{\mathcal{T}_h^i}}{\|\mathbf{v}\|_{H^1(\mathcal{T}_h^i)}}, \quad \forall q \in Q_{T,h},$$

where $\mathbf{V}_h^i = \mathbf{V}_h \cap [H_0^1(\mathcal{T}_h^i)]^n$.

With this assumption we can prove a modified inf-sup condition for $b_{1,h}$, where the defect term can be quantified in terms of the semi-norm induced by the ghost penalty for the total pressure. But first we need to ensure that the corrected Scott-Zhang interpolant π_h^c defined in (4.15) is stable in the ghost-penalty enhanced norm $\|\cdot\|_{\mathbf{V}_h}$.

Lemma 5.2. *For a $v \in H_{\Gamma_d,0}^1(\Omega)$ it holds that*

$$\|\pi_h^c v\|_{\mathbf{V}_h} \lesssim \mu^{1/2} \|v\|_{1,\Omega}.$$

Proof. By definition we have

$$\|\pi_h^c v\|_{\mathbf{V}_h}^2 = \mu \|\varepsilon(\pi_h^c v)\|_{\mathcal{T}_h}^2 + \gamma_u \mu \|h^{-1/2} \pi_h^c v\|_{\Gamma_d}^2 + |\pi_h^c v|_{g_{1,h}}^2.$$

For the first term, the result follows from (4.16), and the stability of π_h . For the second term, since we have $v \in H_{\Gamma_d}^1(\Omega)$ we can write

$$\|h^{-1/2}\pi_h^c v\|_{\Gamma_d} = \|h^{-1/2}(\pi_h^c v - v)\|_{\Gamma_d},$$

and then use the trace inequality (4.2) together with estimate (4.12). The third term follows from the triangle inequality, Assumptions (4.20) and (4.18) for the ghost penalty, and result (4.12).

$$\begin{aligned} |\pi_h^c v|_{g_{1,h}} &\leq |\pi_h^c v - \pi_h v|_{g_{1,h}} + |\pi_h v|_{g_{1,h}} \\ &\leq h^{-1}\mu^{1/2}\|\pi_h^c v - \pi_h v\|_{\mathcal{T}_h} + |\pi_h v|_{g_{1,h}} \\ &\lesssim h^{-1}\mu^{1/2}\|\pi_h^c v - v\|_{\mathcal{T}_h} + h^{-1}\mu^{1/2}\|\pi_h v - v\|_{\mathcal{T}_h} + |\pi_h v|_{g_{1,h}}. \end{aligned}$$

□

With these preparations we can now prove the modified inf-sup condition for $b_{1,h}$.

Lemma 5.3. *Suppose Assumption 5.1 holds, then there exist constants $\beta_1 > 0$ and $\beta_2 > 0$ such that*

$$\sup_{v_h \in \mathbf{V}_h} \frac{b_{1,h}(v_h, q_{T,h})}{\|v_h\|_{\mathbf{V}_h}} \geq \beta_1 \mu^{-1/2} \|q_{T,h}\|_{Q_{T,h}} - \beta_2 \mu^{-1/2} |q_{T,h}|_{g_{2,h}}, \quad \forall q_{T,h} \in Q_{T,h}. \quad (5.9)$$

Proof. Let $q_{T,h} \in Q_{T,h}$ be given, it then exists a $v^q \in \mathbf{H}_{\Gamma_d,0}^1$ such that $-\nabla \cdot v^q = q_{T,h}$ in Ω , and $\beta \|v^q\|_1 \leq \|q_{T,h}\|_{\Omega}$ for a constant $\beta > 0$. Let $v_h^q = \pi_h^c v^q$ where π_h^c is the modified Scott-Zhang interpolator defined in (4.15). After recalling the definition of $b_{1,h}$, an integration by parts and the fact that $v^q = 0$ on Γ_d yields

$$\begin{aligned} b_{1,h}(v_h^q, q_{T,h}) &= -(\nabla \cdot (v_h^q - v^q), q_{T,h})_{\Omega} + ((v_h^q - v^q) \cdot \mathbf{n}, q_{T,h})_{\Gamma_d} - (\nabla \cdot v^q, q_{T,h})_{\Omega} \\ &= ((v_h^q - v^q), \nabla q_{T,h})_{\Omega} - ((v_h^q - v^q) \cdot \mathbf{n}, q_{T,h})_{\Gamma_s} + \|q_{T,h}\|_{\Omega}^2 \end{aligned} \quad (5.10)$$

$$= \text{I} + \text{II} + \|q_{T,h}\|_{\Omega}^2 \geq \text{I} + \text{II} + \|q_{T,h}\|_{\Omega} \|v^q\|_{1,\Omega}. \quad (5.11)$$

Combining the Cauchy-Schwarz inequality with the interpolation estimate (4.7) shows that the first term I can be bounded as

$$|\text{I}| \lesssim \|h^{-1}(v_h^q - v^q)\|_{\Omega} \|h \nabla q_{T,h}\|_{\Omega} \lesssim \|v^q\|_{1,\Omega} \|h \nabla q_{T,h}\|_{\Omega}.$$

Turning to the second term II, we wish to utilize the orthogonality property of the modified Scott-Zhang interpolant by inserting the patch-wise constant pressure $\bar{q}_i = \frac{1}{|\mathcal{P}_i|} (q_{T,h}, 1)_{\mathcal{P}_i}$, leading to

$$\begin{aligned} |\text{II}| &= \left| \sum_{i=1}^N ((v_h^q - v^q) \cdot \mathbf{n}, q_{T,h} - \bar{q}_i)_{\Gamma_s \cap \mathcal{P}_i} \right| \\ &\lesssim \sum_{i=1}^N \|h^{-1/2}(v_h^q - v^q) \cdot \mathbf{n}\|_{\Gamma_s \cap \mathcal{P}_i} \|h^{1/2}(q_{T,h} - \bar{q}_i)\|_{\Gamma_s \cap \mathcal{P}_i} \\ &\lesssim \|v^q\|_1 \|h \nabla q_{T,h}\|_{\mathcal{T}_h} \end{aligned}$$

where in the last line we used (4.8), the trace inequality (4.2) together with the fact that $q_{T,h} - \bar{q}_i$ has zero mean value over \mathcal{P}_i , and thus $\|h^{1/2}(q_{T,h} - \bar{q}_i)\|_{\Gamma_s \cap \mathcal{P}_i} \lesssim \|h \nabla q_{T,h}\|_{\mathcal{T}_h}$. By inserting the bounds for |I| and |II| into (5.11), dividing by $\|v^q\|_{1,\Omega}$ and finally applying the stability of the interpolation operator π_h^c , we deduce that

$$\frac{b_{1,h}(v_h^q, q_{T,h})}{C \|v_h^q\|_{\mathbf{V}_h}} \geq \frac{b_{1,h}(v_h^q, q_{T,h})}{\mu^{1/2} \|v^q\|_{1,\Omega}} \geq \tilde{\beta}_1 \mu^{-1/2} \|q_{T,h}\|_{\Omega} - \tilde{\beta}_2 \mu^{-1/2} (\|h \nabla q_{T,h}\|_{\Omega} - \|h \nabla q_{T,h}\|_{\mathcal{T}_h}),$$

where we assumed that $b_{1,h}(v_h^q, q_{T,h}) \geq 0$ by choosing the sign of v_h^q accordingly. Consequently, we arrive at

$$\sup_{v_h \in \mathbf{V}_h} \frac{b_{1,h}(v_h, q_{T,h})}{\|v_h\|_{\mathbf{V}_h}} \geq \tilde{\beta}_1 \mu^{-1/2} \|q_{T,h}\|_{\Omega} - \tilde{\beta}_2 \mu^{-1/2} \|h \nabla q_{T,h}\|_{\mathcal{T}_h}. \quad (5.12)$$

Next, thanks to (4.22) and Assumption 5.1, there exists a $\mathbf{w}_h \in V_h$ with $\text{supp } \mathbf{w}_h \subset \mathcal{T}_h^i$, such that

$$\|h\nabla q_{T,h}\|_{\mathcal{T}_h} \lesssim \|h\nabla q_{T,h}\|_{\mathcal{T}_h^i} + |q_{T,h}|_{g_{2,h}} \lesssim \sup_{\mathbf{v}_h \in V_h^i} \frac{(\nabla \cdot \mathbf{v}_h, q)_{\mathcal{T}_h^i}}{\|\mathbf{v}_h\|_{H^1(\mathcal{T}_h^i)}} + |q_{T,h}|_{g_{2,h}} \lesssim \sup_{\mathbf{v}_h \in V_h^i} \frac{b_{1,h}(\mathbf{v}_h, q_{T,h})}{\|\mathbf{v}_h\|_{V_h}} + |q_{T,h}|_{g_{2,h}},$$

where in the last step we used that for $\mathbf{v}_h \in V_h^i$ we have $b_{1,h}(\mathbf{v}_h, q_{T,h}) = -(\nabla \cdot \mathbf{v}_h, q_{T,h})_{\mathcal{T}_h^i}$ and the norm equivalence $\|\mathbf{w}_h\|_{H^1(\Omega_h^i)} \approx \|\mathbf{w}_h\|_{V_h}$. In other words, it holds that

$$\sup_{\mathbf{v}_h \in V_h} \frac{b_{1,h}(\mathbf{v}_h, q_{T,h})}{\|\mathbf{v}_h\|_{V_h}} \geq \tilde{\beta}_3 \mu^{-1/2} \|h\nabla q_{T,h}\|_{\mathcal{T}_h} - \tilde{\beta}_4 \mu^{-1/2} |q_{T,h}|_{g_{2,h}}, \quad (5.13)$$

for some positive constants $\tilde{\beta}_3$ and $\tilde{\beta}_4$. Now the inf-sup condition (5.9) follows simply from combining (5.12) and (5.13). \square

Before we turn to the proof of the main inf-sup condition for the total bilinear form $A_h(\cdot, \cdot)$, we want to make the following important remarks.

Remark 5.1 (General inf-sup stable elements). *It is shown in [49] that Assumption 5.1 holds for various mixed finite element spaces with continuous pressure spaces, including generalized Taylor-Hood elements, the Bercovier-Pironneau element and the Mini-element.*

Remark 5.2 (Discontinuous pressure elements). *As shown in [49], inf-sup stable elements with discontinuous pressure spaces can also be used provided that the pressure norm in Assumption 5.1 is modified to include the pressure jump term $h^{1/2} \|\llbracket p_h \rrbracket\|_{\mathcal{F}_h^i(\mathcal{T}_h^i)}$ across interior faces associated with the interior mesh \mathcal{T}_h^i . The integration by parts step in the proof of the intermediate modified inf-sup condition (5.12) will then lead to an additional term of the form $-\tilde{\beta}_5 h^{1/2} \|\llbracket p_h \rrbracket\|_{\mathcal{F}_h^i \cap \Omega}$ on the right-hand side of (5.12). Consequently, the ghost penalty stabilization for the total pressure must then be designed to control this additional term so that*

$$\|h\nabla p_{T,h}\|_{\mathcal{T}_h} + h^{1/2} \|\llbracket p_h \rrbracket\|_{\mathcal{F}_h^i \cap \Omega} \lesssim \|h\nabla p_{T,h}\|_{\Omega_h^i} + |p_{T,h}|_{g_{2,h}} \lesssim \|p_{T,h}\|_{\mathcal{T}_h}, \quad \forall p_{T,h} \in Q_{T,h},$$

holds instead of only (4.22). This is automatically satisfied for the local projection and volume based ghost penalties, as well as for the face-based ghost penalties since we included index $j = 0$ in the summation. As a result, the presented analysis also covers inf-sup stable elements with discontinuous pressure spaces, such as generalized conforming Crouzeix-Raviart elements, the $\mathbb{P}_c^{k+d} - \mathbb{P}_{dc}^k$ elements in $d = 2, 3$ dimensions, and the Bernardi-Raugel element. See [49, Section 6] for details.

Remark 5.3. *The proof of the modified inf-sup condition (5.9) for $b_{1,h}(\cdot, \cdot)$ varies significantly from the one presented in [49]. First, by exploiting the extension property of the total pressure ghost penalty with respect to the h -weighted gradient norm, we avoid the discussion of handling pressure averages with respect to different domains (which is not required in our setting anyhow because of the mixed boundary conditions). On the other hand, our analysis is complicated by the presence of Γ_S mixed boundary conditions, as we now need to handle the boundary terms on Γ_S appearing after integration by parts in (5.10). To translate these terms into a bound involving the h -weighted gradient norm of the pressure, we make use of the orthogonality property of the modified Scott-Zhang interpolant.*

Theorem 5.1. *For all $(\mathbf{u}_h, p_{T,h}, p_{F,h}) \in \mathbf{V}_h \times Q_{T,h} \times Q_{F,h}$ it holds that*

$$\sup_{(\mathbf{v}_h, q_{T,h}, q_{F,h}) \in \mathbf{V}_h \times Q_{T,h} \times Q_{F,h}} \frac{A_h((\mathbf{u}_h, p_{T,h}, p_{F,h}), (\mathbf{v}_h, q_{T,h}, q_{F,h}))}{\|(\mathbf{v}_h, q_{T,h}, q_{F,h})\|_h} \gtrsim \|(\mathbf{u}_h, p_{T,h}, p_{F,h})\|_h. \quad (5.14)$$

Proof. For a given $(\mathbf{u}_h, p_{T,h}, p_{F,h})$ we want to construct functions $(\mathbf{v}_h, q_{T,h}, q_{F,h})$ satisfying

$$A_h((\mathbf{u}_h, p_{T,h}, p_{F,h}), (\mathbf{v}_h, q_{T,h}, q_{F,h})) \gtrsim \|(\mathbf{u}_h, p_{T,h}, p_{F,h})\|_h \|(\mathbf{v}_h, q_{T,h}, q_{F,h})\|_h.$$

Step 1. First, we let $(\mathbf{v}_h, q_{T,h}, q_{F,h}) = (\mathbf{u}_h, -p_{T,h}, -p_{F,h})$, which together with stability results (5.1), (5.2) and the identity

$$a_{2,h}(p_{T,h}, p_{T,h}) - 2b_{2,h}(p_{F,h}, p_{T,h}) + a_{3,h}^2(p_{F,h}, p_{F,h}) = \frac{1}{\lambda} \|p_{T,h} - p_{F,h}\|_{\Omega}^2 + \frac{1}{\lambda} \|p_{F,h}\|_{\Omega}^2,$$

shows that

$$\begin{aligned}
& A_h((\mathbf{u}_h, p_{T,h}, p_{F,h}), (\mathbf{u}_h, -p_{T,h}, -p_{F,h})) \\
&= A_{1,h}(\mathbf{u}_h, \mathbf{u}_h) + A_{2,h}(p_{T,h}, p_{T,h}) - 2b_{2,h}(p_{F,h}, p_{T,h}) + A_{3,h}(p_{F,h}, p_{F,h}) \\
&= A_{1,h}(\mathbf{u}_h, \mathbf{u}_h) + |p_{T,h}|_{g_{2,h}}^2 + \frac{1}{\lambda} \|p_{T,h} - p_{F,h}\|_{\Omega}^2 + \frac{1}{\lambda} \|p_{F,h}\|_{\Omega}^2 + A_{3,h}^1(p_{F,h}, p_{F,h}) + |p_{F,h}|_{g_{3,h}}^2 \\
&\geq c_{A_1} \|\mathbf{u}_h\|_{V_h}^2 + |p_{T,h}|_{g_{2,h}}^2 + c_{A_3} \|p_{F,h}\|_{Q_{F,h}}^2.
\end{aligned} \tag{5.15}$$

Step 2. Next, we choose $\mathbf{v}_h = \mathbf{w}_h$ where \mathbf{w}_h satisfies the modified inf-sup condition (5.9) for $p_{T,h}$ and is rescaled such that $\|\mathbf{w}_h\|_{V_h} = \|p_{T,h}\|_{Q_{T,h}}$. Utilizing (5.1) and (5.9) leads to

$$\begin{aligned}
& A_h((\mathbf{u}_h, p_{T,h}, p_{F,h}), (\mathbf{w}_h, 0, 0)) = A_{1,h}(\mathbf{u}_h, \mathbf{w}_h) + b_{1,h}(\mathbf{w}_h, p_{T,h}) \\
&\geq -C_{A_1} \|\mathbf{u}_h\|_{V_h} \|\mathbf{w}_h\|_{V_h} + \beta_1 \mu^{-1/2} \|p_{T,h}\|_{Q_{T,h}} \|\mathbf{w}_h\|_{V_h} - \beta_2 \mu^{-1/2} |p_{T,h}|_{g_{2,h}} \|\mathbf{w}_h\|_{V_h} \\
&= -C_{A_1} \|\mathbf{u}_h\|_{V_h} \|p_{T,h}\|_{Q_{T,h}} + \beta_1 \mu^{-1/2} \|p_{T,h}\|_{Q_{T,h}}^2 - \beta_2 \mu^{-1/2} |p_{T,h}|_{g_{2,h}} \|p_{T,h}\|_{Q_{T,h}} \\
&\geq -\frac{C_{A_1}}{4\varepsilon} \|\mathbf{u}_h\|_{V_h}^2 + (\beta_1 \mu^{-1/2} - C_{A_1} \varepsilon - \beta_2 \mu^{-1/2} \varepsilon) \|p_{T,h}\|_{Q_{T,h}}^2 - \frac{\beta_2 \mu^{-1/2}}{4\varepsilon} |p_{T,h}|_{g_{2,h}}^2 \\
&\geq -\frac{C_{A_1}(C_{A_1} + \beta_2 \mu^{-1/2})}{2\beta_1 \mu^{-1/2}} \|\mathbf{u}_h\|_{V_h}^2 + \frac{\beta_1 \mu^{-1/2}}{2} \|p_{T,h}\|_{Q_{T,h}}^2 - \frac{\beta_2(C_{A_1} + \beta_2 \mu^{-1/2})}{2\beta_1} |p_{T,h}|_{g_{2,h}}^2,
\end{aligned} \tag{5.16}$$

where in the last 2 steps, an ε -scaled Young's inequality was used together with the choice $\varepsilon = \frac{\beta_1 \mu^{-1/2}}{2(C_{A_1} + \beta_2 \mu^{-1/2})}$.

Step 3. Finally, combining the bounds (5.15) and (5.16), we see that for $\delta > 0$

$$\begin{aligned}
& A_h((\mathbf{u}_h, p_{T,h}, p_{F,h}), (\mathbf{u}_h + \delta \mathbf{w}_h, -p_{T,h}, -p_{F,h})) \geq (c_{A_1} - \delta \frac{C_{A_1}(C_{A_1} + \beta_2 \mu^{-1/2})}{2\beta_1 \mu^{-1/2}}) \|\mathbf{u}_h\|_{V_h}^2 + \delta \frac{\beta_1 \mu^{-1/2}}{2} \|p_{T,h}\|_{Q_{T,h}}^2 \\
&\quad + (1 - \delta \frac{\beta_2(C_{A_1} + \beta_2 \mu^{-1/2})}{2\beta_1}) |p_{T,h}|_{g_{2,h}}^2 + c_{A_3} \|p_{F,h}\|_{Q_{F,h}}^2.
\end{aligned}$$

Choosing $\delta < \min \left\{ \frac{\beta_1 \mu^{-1/2} c_{A_1}}{C_{A_1}(C_{A_1} + \beta_2 \mu^{-1/2})}, \frac{\beta_1}{\beta_2(C_{A_1} + \beta_2 \mu^{-1/2})} \right\}$, we conclude that there is a constant $c_A > 0$ such that

$$\begin{aligned}
& A_h((\mathbf{u}_h, p_{T,h}, p_{F,h}), (\mathbf{u}_h + \delta \mathbf{w}_h, -p_{T,h}, -p_{F,h})) \geq c_A \|\mathbf{u}_h, p_{T,h}, p_{F,h}\|_h^2 \\
&\geq c_A (1 + \delta) \|\mathbf{u}_h, p_{T,h}, p_{F,h}\|_h \|\mathbf{u}_h + \delta \mathbf{w}_h, -p_{T,h}, -p_{F,h}\|_h.
\end{aligned}$$

where in the last step we used that $\|\mathbf{u}_h + \delta \mathbf{w}_h, -p_{T,h}, -p_{F,h}\|_h \leq (1 + \delta) \|\mathbf{u}_h, p_{T,h}, p_{F,h}\|_h$. \square

Corollary 5.1. Method (3.10) has a unique solution satisfying

$$\begin{aligned}
& \|\mathbf{u}_h\|_{V_h} + \|p_{T,h}\|_{Q_{T,h}} + \|p_{F,h}\|_{Q_{F,h}} \lesssim \mu^{-1/2} \|\mathbf{f}\|_{\Omega} + (\mu^{1/2} + 1) \|h^{-1/2} \mathbf{u}_D\|_{\Gamma_d} + \|\sigma_N\|_{\tilde{H}^{-1/2}(\Gamma_s)} \\
&\quad + \lambda^{1/2} \|g\|_{\Omega} + K^{1/2} \|h^{-1/2} p_{F,D}\|_{\Gamma_s} + \|g_N\|_{\tilde{H}^{-1/2}(\Gamma_d)}.
\end{aligned}$$

Proof. Existence and uniqueness follows from Theorem (5.1). For the solution $(\mathbf{u}_h, p_{T,h}, p_{F,h})$ we have

$$\begin{aligned}
& \|\mathbf{u}_h, p_{T,h}, p_{F,h}\|_h \lesssim \sup_{(\mathbf{v}_h, q_{T,h}, q_{F,h}) \in \mathbf{V}_h \times Q_{T,h} \times Q_{F,h}} \frac{A_h((\mathbf{u}_h, p_{T,h}, p_{F,h}), (\mathbf{v}_h, q_{T,h}, q_{F,h}))}{\|(\mathbf{v}_h, q_{T,h}, q_{F,h})\|_h} \\
&= \sup_{(\mathbf{v}_h, q_{T,h}, q_{F,h}) \in \mathbf{V}_h \times Q_{T,h} \times Q_{F,h}} \frac{L_1(\mathbf{v}_h) + L_2(q_{T,h}) + L_3(q_{F,h})}{\|(\mathbf{v}_h, q_{T,h}, q_{F,h})\|_h} \\
&\lesssim \mu^{-1/2} \|\mathbf{f}\|_{\Omega} + (\mu^{1/2} + 1) \|h^{-1/2} \mathbf{u}_D\|_{\Gamma_d} + \|\sigma_N\|_{\tilde{H}^{-1/2}(\Gamma_s)} + \lambda^{1/2} \|g\|_{\Omega} + K^{1/2} \|h^{-1/2} p_{F,D}\|_{\Gamma_s} + \|g_N\|_{\tilde{H}^{-1/2}(\Gamma_d)}.
\end{aligned}$$

\square

5.2. Error estimates

With the inf-sup condition for the total bilinear form $A_h(\cdot, \cdot)$ at hand, an a priori error estimate can now be derived combining a weak Galerkin orthogonality with the approximation properties of the interpolation operator and the weak consistency of the CutFEM stabilization terms.

Lemma 5.4 (Weak Galerkin orthogonality). *Let $(\mathbf{u}, p_T, p_{F,h}) \in H^r(\Omega) \times H^s(\Omega) \times H^t(\Omega)$ be the solution of the Biot problem (3.1), and let $(\mathbf{u}_h, p_{T,h}, p_{F,h}) \in \mathbf{V}_h \times Q_{T,h} \times Q_{F,h}$ be solution of the discrete stabilized formulation (3.10). Then*

$$B_h((\mathbf{u} - \mathbf{u}_h, p_T - p_{T,h}, p_F - p_{F,h}), (\mathbf{v}_h, q_{T,h}, q_{F,h})) = G_h((\mathbf{u}_h, p_{T,h}, p_{F,h}), (\mathbf{v}_h, q_{T,h}, q_{F,h})), \quad (5.17)$$

for all $(\mathbf{v}_h, q_{T,h}, q_{F,h}) \in \mathbf{V}_h \times Q_{T,h} \times Q_{F,h}$.

Theorem 5.2 (A priori error estimate). *Let $(\mathbf{u}, p_T, p_{F,h}) \in H^r(\Omega) \times H^s(\Omega) \times H^t(\Omega)$ be the solution of the Biot problem (3.1), and let $(\mathbf{u}_h, p_{T,h}, p_{F,h}) \in \mathbf{V}_h \times Q_{T,h} \times Q_{F,h}$ be the solution of the discrete stabilized formulation (3.10). Then with $\bar{k} + 1 = \min\{k + 1, r, s\}$ and $\bar{l} + 1 = \min\{l + 1, t\}$ the error $(\mathbf{u} - \mathbf{u}_h, p_T - p_{T,h}, p_F - p_{F,h})$ satisfies*

$$\|(\mathbf{u} - \mathbf{u}_h, p_T - p_{T,h}, p_F - p_{F,h})\|_* \lesssim \mu^{1/2} h^{\bar{k}} |\mathbf{u}|_{\bar{k}+1} + (1 + \lambda^{-1/2} + \lambda^{-1}) h^{\bar{k}} |p_T|_{\bar{k}} + (K^{1/2} h^{\bar{l}} + \lambda^{-1/2} h^{\bar{l}+1} + \lambda^{-1} h^{\bar{l}+1}) |p_F|_{\bar{l}+1}.$$

Proof. The proof follows the usual recipe. We begin by decomposing the error into an interpolation error and a discrete error,

$$\begin{aligned} \|(\mathbf{u} - \mathbf{u}_h, p_T - p_{T,h}, p_F - p_{F,h})\|_* &\lesssim \|(\mathbf{u} - \pi_h \mathbf{u}, p_T - \pi_h p_T, p_F - \pi_h p_F)\|_* + \|(\pi_h \mathbf{u} - \mathbf{u}_h, \pi_h p_T - p_{T,h}, \pi_h p_F - p_{F,h})\|_h \\ &= \|E_\pi\|_* + \|E_h\|_h. \end{aligned}$$

Starting with the E_h term, we take $(\mathbf{v}_h, q_{T,h}, q_{F,h}) = W_h$ which satisfy the inf-sup estimate (5.14) for A_h and scales such that $\|W_h\| = 1$, and utilize the weak Galerkin orthogonality (5.17) to bound the discrete error by the interpolation error and the consistency error of the ghost penalty,

$$\|E_h\|_h \leq A_h(E_h, W_h) = B_h(E_\pi, W_h) + G_h(E_\pi, W_h).$$

Assumption 4.18 regarding weak consistency for the ghost penalties and the chosen scaling yields

$$|E_\pi|_{G_h} \lesssim \mu^{1/2} h^{\bar{k}} |\mathbf{u}|_{\bar{k}+1} + h^{\bar{k}} |p_T|_{\bar{k}} + (K^{1/2} h^{\bar{l}} + \lambda^{-1/2} h^{\bar{l}+1}) |p_F|_{\bar{l}+1}.$$

The bilinear form B_h can be bounded by the results in Lemma 5.1 and the interpolation estimates (4.9),

$$\begin{aligned} B_h(E_\pi, W_h) &\lesssim \|\mathbf{u} - \pi_h \mathbf{u}\|_{V_{h,*}} \|\mathbf{v}_h\|_{V_h} + \|\mathbf{v}_h\|_{V_h} \|p_T - \pi_h p_T\|_{Q_{T,h,*}} + \|\mathbf{u} - \pi_h \mathbf{u}\|_{V_{h,*}} \|q_{T,h}\|_{Q_{T,h}} + \lambda^{-1} \|p_T - \pi_h p_T\|_{Q_{T,h,*}} \|q_{T,h}\|_{Q_{T,h}} \\ &\quad + \lambda^{-1} \|p_F - \pi_h p_F\|_{L^2(\Omega)} \|q_{T,h}\|_{Q_{T,h}} + \lambda^{-1/2} \|p_T - \pi_h p_T\|_{Q_{T,h,*}} \|q_{F,h}\|_{Q_{F,h}} + \|p_F - \pi_h p_F\|_{Q_{F,h,*}} \|q_{F,h}\|_{Q_{F,h}} \\ &\lesssim \mu^{1/2} h^{\bar{k}} |\mathbf{u}|_{\bar{k}+1} + (1 + \lambda^{-1/2} + \lambda^{-1}) h^{\bar{k}} |p_T|_{\bar{k}} + (K^{1/2} h^{\bar{l}} + \lambda^{-1/2} h^{\bar{l}+1} + \lambda^{-1} h^{\bar{l}+1}) |p_F|_{\bar{l}+1}. \end{aligned}$$

□

6. Numerical results

In this section we present numerical results to corroborate the theoretical findings. First, we present a convergence study in 2D, where we vary the parameters λ and K to show that the method is robust in these parameters. Next, we test the geometrical robustness of the method by varying the cut configurations. Afterwards, we present a 3D convergence study, and finally we present an example for solving Biots equations on a brain geometry. In all the following experiments use Taylor-Hood elements for the displacement and total pressure, and second order elements for the fluid pressure, i.e. $k = 2, l = 2$. As ghost-penalty realisations we use the facet-based stabilizations (4.21), with stabilization parameters $\gamma_1 = 0.1, \gamma_2 = 0.01$, and Nitsche parameters $\gamma_u = \gamma_p = 40.0$. All implementation is done in the Julia based open-source library Gridap [78, 79], with plugins GridapEmbedded, GridapPETSc, and STLCutters [80], and all experiments are run with Julia version 1.11.2.

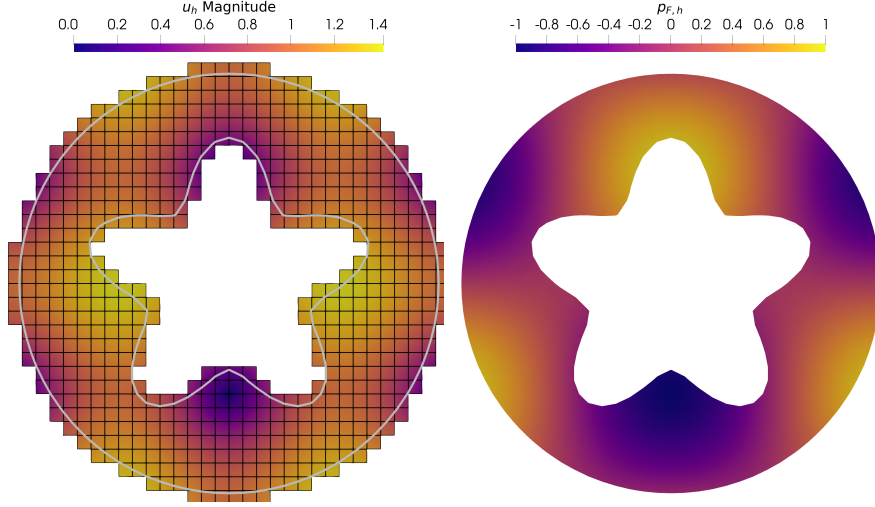


Figure 6.1: The displacement solution \mathbf{u}_h (magnitude) on the full computational domain and the fluid pressure solution $p_{F,h}$ on the physical domain for $N = 32$ and $\lambda = 1$ and $K = 1$.

6.1. Convergence analysis

We begin with a convergence analysis and define the background domain $\tilde{\Omega} = [-1, 1]^2$, the circle

$$\tilde{\Omega}_1 = \{(x, y) \in \mathbb{R}^2 : x^2 + y^2 < 0.95^2\},$$

and a flower-like domain

$$\tilde{\Omega}_2 = \{(x, y) \in \mathbb{R}^2 : \phi(x, y) < 0\}, \quad \phi(x, y) = \sqrt{x^2 + y^2} - r_0 - r_1 \cos(5.0 \operatorname{atan}_2(y, x)),$$

with $r_0 = 0.7$, $r_1 = 0.18$. The computational domain is defined as

$$\Omega = \tilde{\Omega}_1 \setminus \tilde{\Omega}_2, \quad \Gamma_d = \partial\tilde{\Omega}_1, \quad \Gamma_s = \partial\tilde{\Omega}_2,$$

i.e. a circle with a flower hole in it see Figure 6.1 for an illustration.

The problem is solved on a uniform mesh consisting of N^2 uniform square elements, where the element size h_n is gradually decreased by refining the mesh, setting $N = 2^{2+n}$, with $n = 2, \dots, 6$. For each refinement, the corresponding error E_n for the three unknowns are calculated in related norms, and the experimental order of convergence (EOC) is calculated via

$$\text{EOC} = \frac{\log(E_{n-1}/E_n)}{\log(h_{n-1}/h_n)}.$$

We use the following exact solutions

$$\begin{aligned} \mathbf{u}_{\text{ex}}(x, y) &= \begin{bmatrix} \cos(\pi y) \\ \sin(\pi x) \end{bmatrix} \\ p_{F,\text{ex}}(x, y) &= \sin(\pi x) \sin(\pi y), \\ p_{T,\text{ex}}(x, y) &= p_{F,\text{ex}}(x, y) - \lambda \nabla \cdot \mathbf{u}_{\text{ex}}(x, y), \end{aligned}$$

and define the terms on the right hand side, f and g correspondingly. We vary the parameters $\lambda = \{1, 10^8\}$, $K = \{1, 10^{-8}\}$, for each refinement series, while letting $\mu = 1$. One solution is depicted in Figure 6.1. The convergence results are shown in Figure 6.2. We observe optimal convergence rates, also when λ is large, and K is small. Note that the discrete norm for $p_{F,h}$ (3.8) is scaled by K and $1/\lambda$.

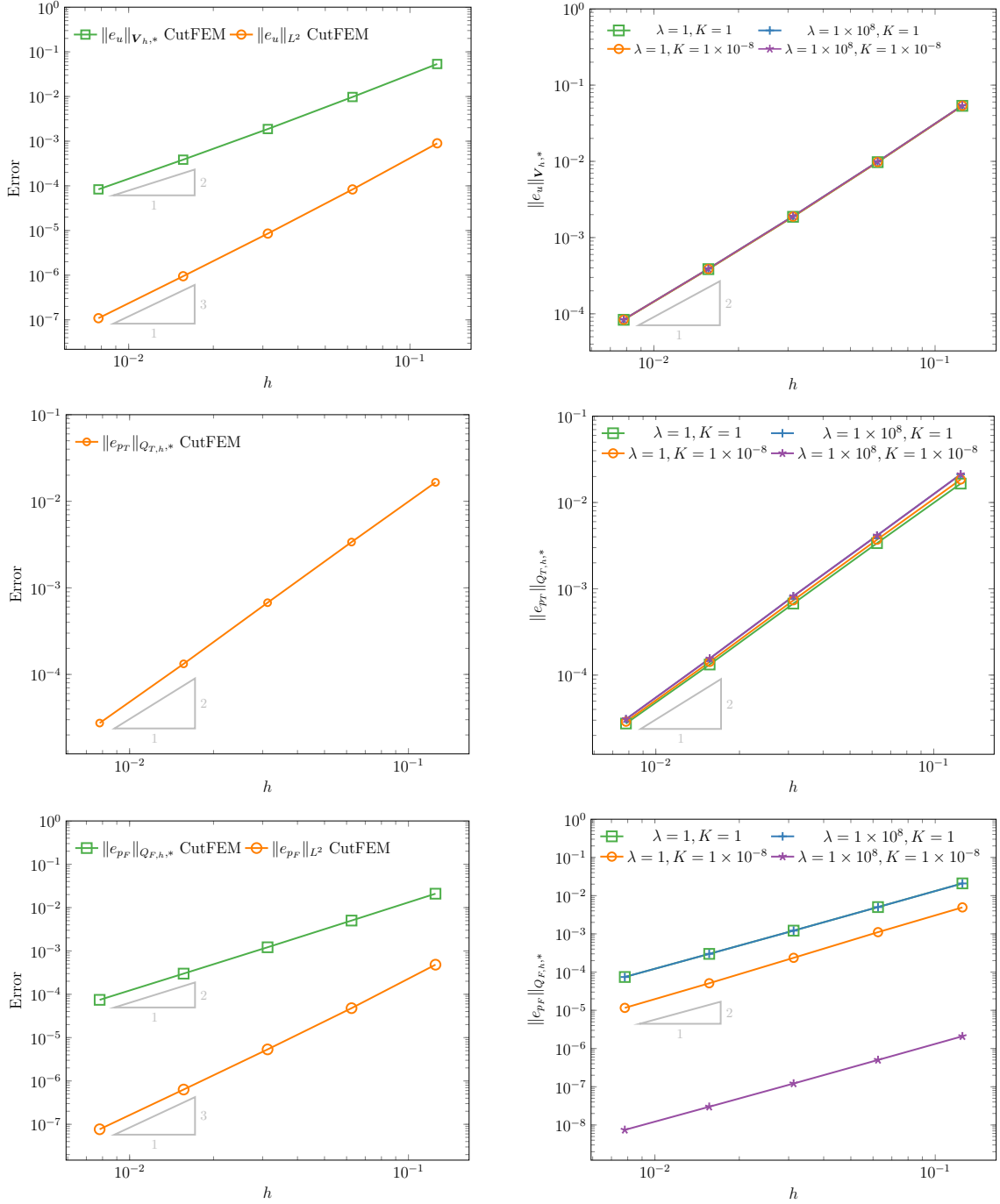


Figure 6.2: Convergence rates. Left: Errors measured in both the discrete norms (3.6)-(3.8) and L^2 -norm for $\lambda = 1$ and $K = 1$. Right: Errors measured in the discrete norms for different values of λ and K .

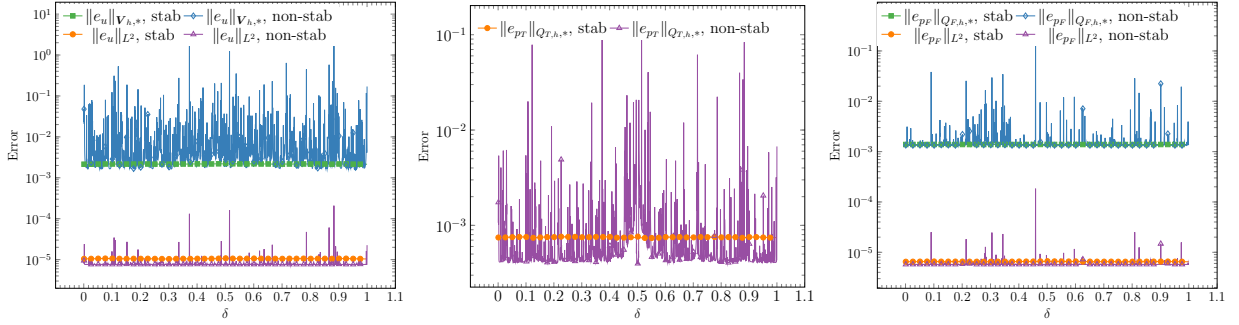


Figure 6.3: Sensitivity analysis. Errors in both the discrete norms (3.6)-(3.8) and L^2 -norm for different cut configurations with and without stabilization.

6.2. Geometrical robustness

Next, we test the robustness of the method with respect to different cut configurations. We repeat the setup from the convergence analysis, and fix $N = 60$ and let $\lambda = K = \mu = 1$. By slightly moving $\bar{\Omega}$, we generate a family of translated background domains $\{\bar{\Omega}_{\delta_k}\}_{k=1}^{2000}$ such that $\bar{\Omega}_{\delta_k} = [-1 + \delta_k h, 1 + \delta_k h]^2$ with $\delta_k = k \cdot 5 \cdot 10^{-4}$. We calculate the errors for each different cut configurations with and without stabilization terms. We see that for the non-stabilized formulations, the error in the discrete norms (3.6)-(3.8) are very sensitive to the cut configuration, while the stabilized formulation is robust with respect to the cut configuration. For the error in the L^2 -norm, there are also some sensitivity for the non-stabilized formulation.

6.3. Convergence analysis 3D

Finally, we test the method in 3D, and now representing the physical domain with by STL mesh. We define the background domain as $\bar{\Omega} = [-1.3, 1.3]^3$. The STL mesh consists of a popcorn-like domain with a spherical hole in it, see figure 6.4. The exact solution is defined by

$$\mathbf{u}_{\text{ex}}(x, y, z) = \begin{bmatrix} \sin(\pi x) \cos(\pi y) \\ \sin(\pi z) \\ \cos(\pi x) \sin(\pi y) \sin(\pi z) \end{bmatrix}$$

$$p_{F,\text{ex}}(x, y, z) = \cos(\pi x) \sin(\pi x) \sin(\pi y),$$

$$p_{T,\text{ex}}(x, y, z) = p_{F,\text{ex}}(x, y) - \lambda \nabla \cdot \mathbf{u}_{\text{ex}}(x, y),$$

We let $\lambda = 5$, $\mu = 1$ and $K = 0.1$, and use a uniform mesh with N^3 elements, where the element size h_n is gradually decreased by refining the mesh, setting $N = [12, 24, 48]$. The convergence results are seen in Table 6.1, and illustrations of the results in Figure 6.4. We observe higher convergence than optimal convergence rates, which we assume is due to the geometrical resolution.

6.4. Poroelastic simulations of brain mechanics

In the final example we will consider the interstitial fluid flow and brain tissue deformation when considering a poroelastic model of the brain under a setting with mixed boundary conditions. Interstitial fluid flow caused by poroelastic deformations is interesting in the context of the glymphatic system [81], see [82] for a recent review. In particular, an issue that has been debated is whether there are any static pressure driven advection [83] acting on long time scales. In the present context we therefore put focus on static forces represented by mixed boundary conditions. Here, we consider the situation of a brain mostly floating in cerebrospinal fluid while parts are attached to the dura. Specifically, it is known that while the intracranial pressure of the CSF pulsate with cardiac pulsation as well as the respiration of magnitudes of 100-1000 Pa, the pulsation is largely synchronous throughout the whole brain [84]. Therefore we ignore the pulsation and instead consider a small spatial gradients of 1 Pa / cm [3, 85]. Furthermore, as highlighted in studies of traumatic head injuries, dura mater attachment prevent local motion and

Table 6.1: Errors and experimental orders of convergence (EOC) for the 3-dimensional analysis.

N	$\ u - u_h\ _{V_{h,*}}$	EOC	$\ u - u_h\ _{L^2}$	EOC	$\ p_T - p_{T,h}\ _{Q_{T,h,*}}$	EOC
12	1.57	–	1.62×10^{-1}	–	1.15	–
24	1.89×10^{-1}	3.05	8.56×10^{-3}	4.25	2.30×10^{-1}	2.32
48	4.21×10^{-2}	2.17	6.85×10^{-4}	3.64	4.89×10^{-2}	2.23

N	$\ p_F - p_{F,h}\ _{Q_{F,h,*}}$	EOC	$\ p_F - p_{F,h}\ _{L^2}$	EOC
12	6.03×10^{-2}	–	2.41×10^{-2}	–
24	7.38×10^{-3}	3.03	1.13×10^{-3}	4.42
48	1.61×10^{-3}	2.19	6.11×10^{-5}	4.21

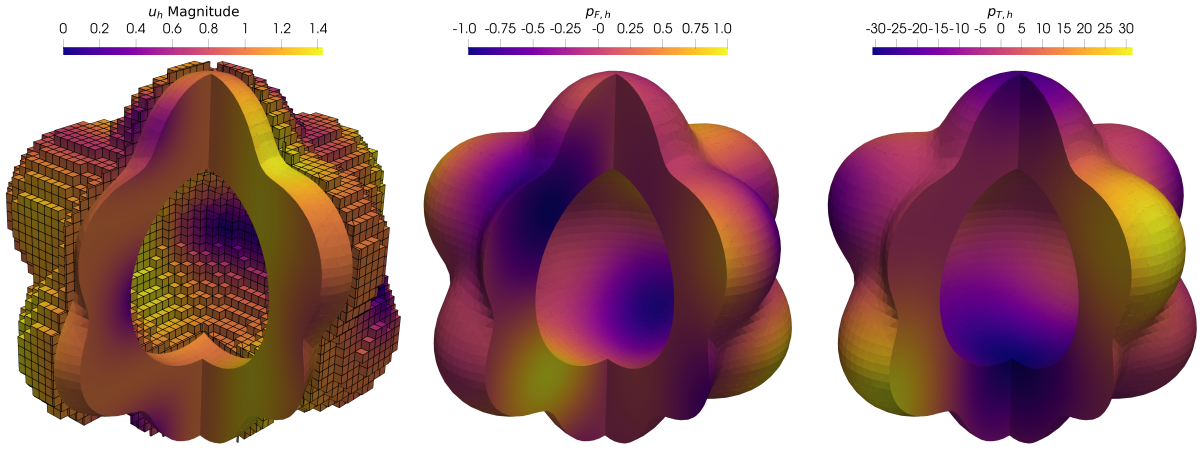


Figure 6.4: The computational domain and the displacement solution u_h (magnitude), the fluid pressure solution $p_{F,h}$, and the total pressure solution $p_{T,h}$ for $N = 48$, here with a section removed for illustration.

henceforth we consider dura attachment along the tentorium, see Fig 6.5, as a homogeneous Dirichlet condition for the displacement along with null flux. Elsewhere we assign a vertical pressure gradient, see e.g. [86, 87] for more detailed pressure characterizations. Given such a setup situation, it is interesting to quantify the flow, pressure and displacement. Specifically, we solve system (2.1) - (2.3) on a right brain hemisphere, represented by surface STL mesh available at [88]. In the background mesh we set a mesh size of $h = 2.8125$ mm, giving the resulting system 1 million degrees of freedom. As boundary conditions we set

$$\begin{aligned}
 \mathbf{u}_D &= 0 && \text{on tentorium,} \\
 g_N &= 0 && \text{on tentorium,} \\
 \boldsymbol{\sigma}_N &= -p_{F,D}\mathbf{n} && \text{on cerebrum,} \\
 p_{F,D}(x, y, z) &= 1.33 - (z_0 - z)1.33 \times 10^{-3} && \text{on cerebrum,}
 \end{aligned}$$

where z_0 is the minimum z-coordinate of the domain. Parameters were set to $E = 1600$ Pa, $\nu = 0.499$, and $K = 2.0 \times 10^{-6}$ mm² Pa⁻¹, see [3], and all source terms were set to zero. For the Nitsche parameter for the fluid pressure we have chosen the value higher than usual ($\gamma_p = 4.0 \times 10^6$) to better enforce the boundary condition on this relatively coarse mesh, as the dynamics are mainly driven by the gradient of the boundary pressure. As shown in Fig 6.5 the displacement are of the order 0.1 mm which is similar to that reported in the literature and through magnetic resonance imaging [89]. The displacement field is however much more complex in real life, it varies a lot between individuals, and are caused by multiple causes such as cardiac, respiratory, sleep etc [90]. Concerning the interstitial fluid velocities, several studies have attempted to assess them in particular because of their importance for

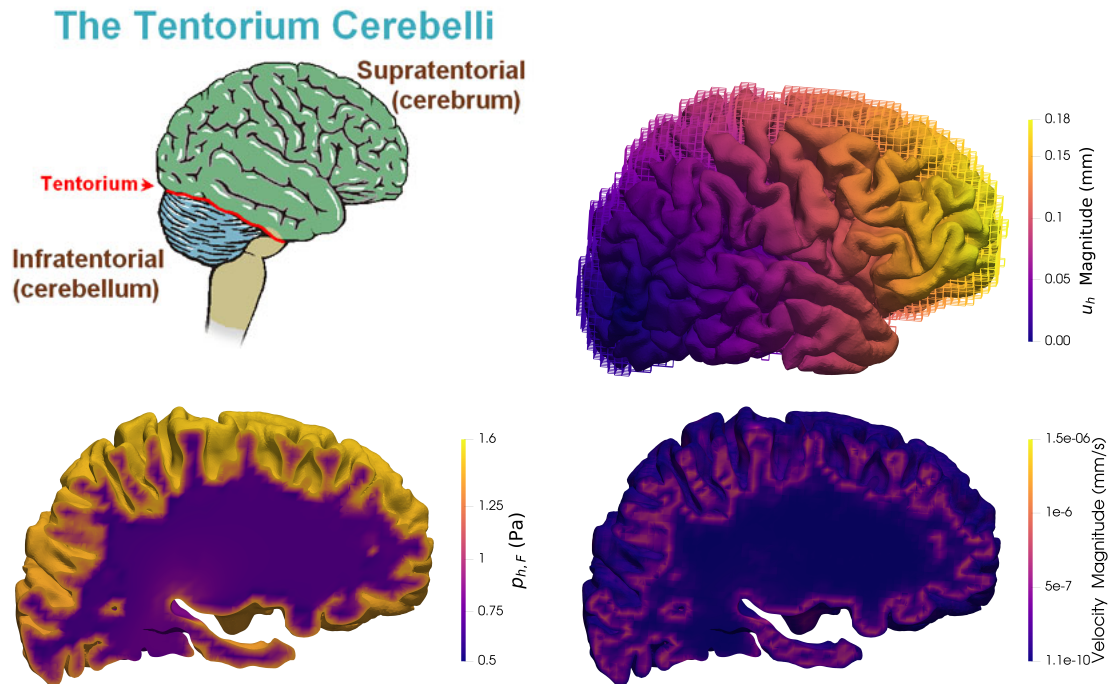


Figure 6.5: An illustration ²(left, top) of the cerebellum, cerebrum and the tentorium that separate these different parts of the central nervous system. The tentorium a part of the dura matter and in the following simulations we simulate the case of attachment to the tentorium via homogenous Dirichlet conditions in that region. Otherwise the brain is subjected to a stress field in the z-direction. The corresponding displacement (right, top) is shown to be of a magnitude of almost 0.1 mm. The pressure gradients are localized to boundaries (left, bottom) as are the highest fluid velocities (right, bottom). Displacement field is shown together with the (clipped) background mesh.

the glymphatic system. For example, [83] estimated pore velocities of up to 100 nm/s computationally, whereas [91] estimated a superficial velocity of $\mu\text{m/s}$. Furthermore, in a parameter estimating study, [92], superficial velocities of the order of 2-4 μmin was found to provide a best fit for overnight MRI-tracer movement. Our estimates here are at the lower end of the spectrum, with maximal velocities of the order of nm/s. We do remark that the static pressure gradient employed in our setting is relatively to the intracranial pressure pulsation occurring due to cardiac pulsation or respiration.

7. Conclusion and outlook

We have presented a stabilized cut finite element method for the Biot system based on the total-pressure formulation. Our theoretical analysis established stability and optimal convergence rates, independent of physical parameters and cut configurations, and these properties were confirmed by extensive numerical experiments in two and three dimensions. The CutFEM approach enables robust simulation of poroelasticity in complex domains, such as brain mechanics, without the need for body-fitted meshes.

Efficient preconditioners are essential for solving the Biot system at large scale, and future work should include the development and analysis of preconditioners for the proposed CutFEM formulation, e.g., based on [21]. Additional directions include octree-based parallel adaptive mesh refinement [93] for which Gridap already provides an extension module. This would allow for local refinement along the embedded boundary, and better resolution of boundary dynamics. Moreover, the geometric and discretization algorithms needs to be extended to account for multiple interfaces

²https://en.wikipedia.org/wiki/Cerebellar_tentorium, license: public domain

and heterogeneous brain regions in more realistic multiphysic brain models with spatially varying material parameters. Other interesting multiphysic settings that could be considered are Biot-Stokes coupling [94] to include couplings with the surrounding CSF flow, or multiple-network poroelasticity (MPET) equations [95]. A main advantage of the CutFEM approach in the context of biomedical applications is that meshing [96, 97] is avoided, while still sub-voxel resolution of surfaces are retained through imaging segmentation tools such as for example FreeSurfer.

Acknowledgements

NB acknowledges support from the Swedish Research Council under grant no. 2021-06594 while in residence at Institut Mittag-Leffler in Djursholm, Sweden during the fall semester of 2025. KAM acknowledges funding by: Stiftelsen Kristian Gerhard Jebsen via the K. G. Jebsen Centre for Brain Fluid Research; the national infrastructure for computational science in Norway Sigma2 via grant NN9279K; the Center of Advanced Study at the Norwegian Academy of Science and Letters under the program Mathematical Challenges in Brain Mechanics; research stay funds at ICERM, Brown under the program Numerical PDEs: Analysis, Algorithms, and Data Challenges; the Computational Hydrology project, a strategic Sustainability initiative at the Faculty of Natural Sciences, UiO; and the grant 101141807 (aCleanBrain) by the European Research Council. AM acknowledges travel funds from: ICERM, Brown under the program "Numerical PDEs: Analysis, Algorithms, and Data Challenges"; Norwegian Academy of Science and Letters under the program "Mathematical Challenges in Brain Mechanics"; Institut Mittag-Leffler in Djursholm, Sweden, under the research program "Interfaces and unfitted discretization methods (grant no. 2021-06594 from the Swedish Research Council).

References

- [1] M. A. Biot, General theory of three-dimensional consolidation, *J. Appl. Phys.* 12 (2) (1941) 155–164.
- [2] K.-H. Støverud, Relation between the Chiari I malformation and syringomyelia from a mechanical perspective, Ph.D. thesis (2014).
- [3] K. H. Støverud, M. Alnæs, H. P. Langtangen, V. Haughton, K.-A. Mardal, Poro-elastic modeling of Syringomyelia—a systematic study of the effects of pia mater, central canal, median fissure, white and gray matter on pressure wave propagation and fluid movement within the cervical spinal cord, *Comput. Methods Biomech. Biomed. Engin.* 19 (6) (2016) 686–698.
- [4] A. Malandrino, E. Moendarbary, Poroelasticity of living tissues, *Encycl. Biomed. Eng.* (2019) 238–245.
- [5] M. Bukac, I. Yotov, R. Zakerzadeh, P. Zunino, Effects of poroelasticity on fluid-structure interaction in arteries: A computational sensitivity study, in: A. Quarteroni (Ed.), *Modeling the Heart and the Circulatory System*, Vol. 14, Springer International Publishing, Cham, 2015, pp. 197–220.
- [6] K. H. Støverud, M. Darcis, R. Helmig, S. M. Hassanizadeh, Modeling concentration distribution and deformation during convection-enhanced drug delivery into brain tissue, *Transp Porous Med* 92 (1) (2012) 119–143.
- [7] G. Gambolati, P. Teatini, D. Baú, M. Ferronato, Importance of poroelastic coupling in dynamically active aquifers of the Po River Basin, Italy, *Water Resour. Res.* 36 (9) (2000) 2443–2459.
- [8] S. Salimzadeh, T. Usui, A. Paluszny, R. W. Zimmerman, Finite element simulations of interactions between multiple hydraulic fractures in a poroelastic rock, *Int. J. Rock Mech. Min. Sci.* 99 (2017) 9–20.
- [9] H. Wang, *Theory of Linear Poroelasticity with Applications to Geomechanics and Hydrogeology*, Vol. 2, Princeton university press, 2000.
- [10] A. H.-D. Cheng, *Poroelasticity*, Vol. 27 of *Theory and Applications of Transport in Porous Media*, Springer International Publishing, Cham, 2016.

- [11] M. A. Murad, A. F. D. Loula, Improved accuracy in finite element analysis of Biot's consolidation problem, *Comput. Methods Appl. Mech. Engrg.* 95 (3) (1992) 359–382.
- [12] C. Rodrigo, F. J. Gaspar, X. Hu, L. T. Zikatanov, Stability and monotonicity for some discretizations of the Biot's consolidation model, *Comput. Methods Appl. Mech. Engrg.* 298 (2016) 183–204.
- [13] P. J. Phillips, M. F. Wheeler, A coupling of mixed and continuous Galerkin finite element methods for poroelasticity. I. The continuous in time case, *Comput. Geosci.* 11 (2) (2007) 131–144.
- [14] C. Rodrigo, X. Hu, P. Ohm, J. H. Adler, F. J. Gaspar, L. T. Zikatanov, New stabilized discretizations for poroelasticity and the Stokes' equations, *Comput. Methods Appl. Mech. Engrg.* 341 (2018) 467–484.
- [15] S.-Y. Yi, A study of two modes of locking in poroelasticity, *SIAM J. Numer. Anal.* 55 (4) (2017) 1915–1936.
- [16] X. Hu, C. Rodrigo, F. J. Gaspar, L. T. Zikatanov, A nonconforming finite element method for the Biot's consolidation model in poroelasticity, *J. Comput. Appl. Math.* 310 (2017) 143–154.
- [17] J. J. Lee, Robust three-field finite element methods for Biot's consolidation model in poroelasticity, *BIT* 58 (2) (2018) 347–372.
- [18] S.-Y. Yi, A coupling of nonconforming and mixed finite element methods for Biot's consolidation model, *Numer. Methods Partial Differential Equations* 29 (5) (2013) 1749–1777.
- [19] P. J. Phillips, M. F. Wheeler, A coupling of mixed and discontinuous Galerkin finite-element methods for poroelasticity, *Comput. Geosci.* 12 (4) (2008) 417–435.
- [20] M. F. Wheeler, G. Xue, I. Yotov, Coupling multipoint flux mixed finite element methods with continuous Galerkin methods for poroelasticity, *Comput. Geosci.* 18 (1) (2014) 57–75.
- [21] J. J. Lee, K.-A. Mardal, R. Winther, Parameter-robust discretization and preconditioning of Biot's consolidation model, *SIAM J. Sci. Comput.* 39 (1) (2017) A1–A24.
- [22] R. Oyarzúa, R. Ruiz-Baier, Locking-free finite element methods for poroelasticity, *SIAM J. Numer. Anal.* 54 (5) (2016) 2951–2973.
- [23] S.-Y. Yi, Convergence analysis of a new mixed finite element method for Biot's consolidation model, *Numer. Methods Partial Differential Equations* 30 (4) (2014) 1189–1210.
- [24] J. J. Lee, Robust error analysis of coupled mixed methods for Biot's consolidation model, *J. Sci. Comput.* 69 (2) (2016) 610–632.
- [25] I. Ambartsumyan, E. Khattatov, I. Yotov, A coupled multipoint stress–multipoint flux mixed finite element method for the Biot system of poroelasticity, *Comput. Methods Appl. Mech. Engrg.* 372 (2020) 113407.
- [26] N. Moës, J. Dolbow, T. Belytschko, A finite element method for crack growth without remeshing, *Int. J. Numer. Meth. Engng.* 46 (1) (1999) 131–150.
- [27] T.-P. Fries, T. Belytschko, The extended/generalized finite element method: An overview of the method and its applications, *Int. J. Numer. Methods Eng.* 00 (2000) 1–6.
- [28] J. Chessa, T. Belytschko, An extended finite element method for two-phase fluids, *J. Appl. Mech.* 70 (1) (2003) 10–17.
- [29] A. Hansbo, P. Hansbo, An unfitted finite element method, based on Nitsche's method, for elliptic interface problems, *Comput. Methods Appl. Mech. Engrg.* 191 (47–48) (2002) 5537–5552.
- [30] A. Fumagalli, Numerical modelling of flows in fractured porous media by the XFEM method, Ph.D. thesis, Italy (2012).

- [31] A. Fumagalli, A. Scotti, An efficient XFEM approximation of Darcy flows in arbitrarily fractured porous media, *Oil Gas Sci. Technol. IFP Energ. Nouv.* 69 (4) (2014) 555–564.
- [32] E. Burman, S. Claus, P. Hansbo, M. G. Larson, A. Massing, CutFEM: Discretizing geometry and partial differential equations, *Internat. J. Numer. Methods Engrg.* 104 (7) (2015) 472–501.
- [33] F. de Prenter, C. V. Verhoosel, E. H. van Brummelen, M. G. Larson, S. Badia, Stability and conditioning of immersed finite element methods: Analysis and remedies, *Arch Comput. Methods Eng* (2023).
- [34] J. Nitsche, über ein variationsprinzip zur lösung von dirichlet-problemen bei verwendung von teilräumen, die keinen randbedingungen unterworfen sind, *Abh. Aus Dem Math. Semin. Univ. Hambg.* 36 (1) (1971) 9–15.
- [35] E. Burman, P. Hansbo, Fictitious domain finite element methods using cut elements: II. A stabilized Nitsche method, *Appl. Numer. Math.* 62 (4) (2012) 328–341.
- [36] E. Burman, P. Hansbo, Fictitious domain finite element methods using cut elements: I. A stabilized Lagrange multiplier method, *Comput. Methods Appl. Mech. Engrg.* 199 (41-44) (2010) 2680–2686.
- [37] A. Johansson, M. Larson, A high order discontinuous Galerkin Nitsche method for elliptic problems with fictitious boundary, *Numer. Math.* 123 (4) (2013) 607–628.
- [38] S. Badia, F. Verdugo, A. F. Martín, The aggregated unfitted finite element method for elliptic problems, *Comput. Methods Appl. Mech. Engrg.* 336 (2018) 533–553.
- [39] E. Burman, P. Zunino, Numerical approximation of large contrast problems with the unfitted nitsche method, in: J. Blowey, M. Jensen (Eds.), *Frontiers in Numerical Analysis - Durham 2010*, Springer, Berlin, Heidelberg, 2012, pp. 227–282.
- [40] J. Guzmán, M. A. Sánchez, M. Sarkis, A finite element method for high-contrast interface problems with error estimates independent of contrast, *J Sci Comput* 73 (1) (2017) 330–365.
- [41] C. Gürkan, A. Massing, A stabilized cut discontinuous Galerkin framework for elliptic boundary value and interface problems, *Comput. Methods Appl. Mech. Engrg.* 348 (2019) 466–499.
- [42] E. Burman, P. Hansbo, Fictitious domain methods using cut elements: III. A stabilized Nitsche method for Stokes’ problem, *ESAIM Math Model Numer Anal* 48 (3) (2014) 859–874.
- [43] A. Massing, M. G. Larson, A. Logg, M. E. Rognes, A stabilized Nitsche overlapping mesh method for the Stokes problem, *Numer. Math.* 128 (1) (2014) 73–101.
- [44] E. Burman, S. Claus, A. Massing, A stabilized cut finite element method for the three field Stokes problem, *SIAM J. Sci. Comput.* 37 (4) (2015) A1705–A1726.
- [45] L. Cattaneo, L. Formaggia, G. F. Iori, A. Scotti, P. Zunino, Stabilized extended finite elements for the approximation of saddle point problems with unfitted interfaces, *Calcolo* (2014) 1–30.
- [46] A. Massing, B. Schott, W. Wall, A stabilized Nitsche cut finite element method for the Oseen problem, *Comput. Methods Appl. Mech. Engrg.* 328 (2018) 262–300.
- [47] M. Winter, B. Schott, A. Massing, W. A. Wall, A Nitsche cut finite element method for the Oseen problem with general Navier boundary conditions, *Comput. Methods Appl. Mech. Engrg.* 330 (2017) 220–252.
- [48] S. Badia, A. F. Martín, F. Verdugo, Mixed aggregated finite element methods for the unfitted discretization of the Stokes problem, *SIAM J. Sci. Comput.* 40 (6) (2018) B1541–B1576.
- [49] J. Guzmán, M. Olshanskii, Inf-sup stability of geometrically unfitted Stokes finite elements, *Math. Comp.* 87 (313) (2018) 2091–2112.

- [50] J. S. Dokken, A. Johansson, A. Massing, S. W. Funke, A multimesh finite element method for the Navier–Stokes equations based on projection methods, *Comput. Methods Appl. Mech. Engrg.* 368 (2020) 113129.
- [51] E. Burman, S. Frei, A. Massing, Eulerian time-stepping schemes for the non-stationary Stokes equations on time-dependent domains, *Numer. Math.* 150 (2022) 1–56.
- [52] B. Schott, U. Rasthofer, V. Gravemeier, W. A. Wall, A face-oriented stabilized Nitsche-type extended variational multiscale method for incompressible two-phase flow, *Int. J. Numer. Methods Eng.* 104 (7) (2015) 721–748.
- [53] S. Claus, P. Kerfriden, A CutFEM method for two-phase flow problems, *Comput. Methods Appl. Mech. Engrg.* (2019).
- [54] T. Frachon, S. Zahedi, A cut finite element method for incompressible two-phase Navier-Stokes flows, *J. Comp. Phys.* 384 (2019) 77–98.
- [55] A. Massing, M. G. Larson, A. Logg, M. Rognes, A Nitsche-based cut finite element method for a fluid-structure interaction problem, *Commun. Appl. Math. Comput. Sci.* 10 (2) (2015) 97–120.
- [56] N. Berre, M. E. Rognes, A. Massing, Cut finite element discretizations of cell-by-cell EMI electrophysiology models, *SIAM J. Sci. Comput.* 46 (4) (2024) B527–B553.
- [57] T. Frachon, P. Hansbo, E. Nilsson, S. Zahedi, A divergence preserving cut finite element method for Darcy flow, *SIAM J. Sci. Comput.* 46 (3) (2024) A1793–A1820.
- [58] C. Lehrenfeld, T. van Beeck, I. Voulis, Analysis of divergence-preserving unfitted finite element methods for the mixed Poisson problem, *Mathematics of Computation* 94 (354) (2025) 1667–1699.
- [59] P. Hansbo, M. G. Larson, A. Massing, A stabilized cut finite element method for the Darcy problem on surfaces, *Comput. Methods Appl. Math.* 326 (2017) 298–318.
- [60] B. Flemisch, A. Fumagalli, A. Scotti, A review of the XFEM-Based approximation of flow in fractured porous media, in: *Advances in Discretization Methods: Discontinuities, Virtual Elements, Fictitious Domain Methods*, Vol. 12, Springer, 2016, pp. 47–76.
- [61] C. D’Angelo, A. Scotti, A mixed finite element method for Darcy flow in fractured porous media with non-matching grids, *ESAIM Math Model Numer Anal* 46 (02) (2012) 465–489.
- [62] L. Formaggia, A. Fumagalli, A. Scotti, P. Ruffo, A reduced model for Darcy’s problem in networks of fractures, *ESAIM Math Model Numer Anal* 48 (4) (2013) 1089–1116.
- [63] M. Del Pra, A. Fumagalli, A. Scotti, Well posedness of fully coupled fracture/bulk Darcy flow with XFEM, *SIAM J. Numer. Anal.* 55 (2) (2017) 785–811.
- [64] E. Burman, P. Hansbo, M. G. Larson, K. Larsson, Cut finite elements for convection in fractured domains, *Comput. Fluids* 179 (2019) 726–734.
- [65] S. Bordas, E. Burman, M. Larson, M. Olshanskii (Eds.), *Geometrically Unfitted Finite Element Methods and Applications*, Springer, 2018.
- [66] A. Main, G. Scovazzi, The shifted boundary method for embedded domain computations. Part I: Poisson and Stokes problems, *J. Comput. Phys.* 372 (2018) 972–995.
- [67] D. Cerroni, F. A. Radu, P. Zunino, Numerical solvers for a poromechanic problem with a moving boundary, *Math. Eng.* 1 (4) (2019) 824–848.
- [68] Z. Liu, Y. Zhang, Y. Jiang, H. Yang, Y. Yang, Unfitted finite element method for fully coupled poroelasticity with stabilization, *Comput. Methods Appl. Mech. Engrg.* 397 (2022) Paper No. 115132, 31.

- [69] C. Ager, B. Schott, M. Winter, W. A. Wall, A Nitsche-based cut finite element method for the coupling of incompressible fluid flow with poroelasticity, *Comput. Methods Appl. Mech. Engrg.* 351 (2019) 253–280.
- [70] A. Massing, M. G. Larson, A. Logg, M. E. Rognes, A stabilized Nitsche fictitious domain method for the Stokes problem, *J. Sci. Comput.* 61 (3) (2014) 604–628.
- [71] R. Becker, E. Burman, P. Hansbo, A Nitsche extended finite element method for incompressible elasticity with discontinuous modulus of elasticity, *Comput. Methods Appl. Mech. Engrg.* 198 (41-44) (2009) 3352–3360.
- [72] S. C. Brenner, Korn’s inequalities for piecewise H^1 vector fields, *Math. Comp.* 73 (247) (2004) 1067–1087.
- [73] S. C. Brenner, Poincaré-Friedrichs inequalities for piecewise H^1 functions, *SIAM J. Numer. Anal.* 41 (1) (2003) 306–324.
- [74] E. M. Stein, *Singular Integrals and Differentiability Properties of Functions*, Princeton University Press, 1970.
- [75] E. Burman, Ghost penalty, *C. R. Acad. Sci. Paris* 348 (21-22) (2010) 1217–1220.
- [76] W. E. H. Sollie, O. Bokhove, J. J. W. van der Vegt, Space–time discontinuous Galerkin finite element method for two-fluid flows, *J. Comput. Phys.* 230 (3) (2011) 789–817.
- [77] J. Preuß, Higher order unfitted isoparametric space-time FEM on moving domains, Ph.D. thesis, NAM, University of Göttingen (2018).
- [78] S. Badia, F. Verdugo, Gridap: An extensible finite element toolbox in julia, *J. Open Source Softw.* 5 (52) (2020) 2520.
- [79] F. Verdugo, S. Badia, The software design of Gridap: A Finite Element package based on the Julia JIT compiler, *Comput. Phys. Commun.* 276 (2022) 108341.
- [80] S. Badia, P. A. Martorell, F. Verdugo, Geometrical discretisations for unfitted finite elements on explicit boundary representations, *J. Comput. Phys.* 460 (2022) 111162.
- [81] J. J. Iliff, M. Wang, Y. Liao, B. A. Plogg, W. Peng, G. A. Gundersen, H. Benveniste, G. E. Vates, R. Deane, S. A. Goldman, et al., A paravascular pathway facilitates CSF flow through the brain parenchyma and the clearance of interstitial solutes, including amyloid β , *Sci. Transl. Med.* 4 (147) (2012) 147ra111–147ra111.
- [82] T. Bohr, P. G. Hjorth, S. C. Holst, S. Hrabětová, V. Kiviniemi, T. Lilius, I. Lundgaard, K.-A. Mardal, E. A. Martens, Y. Mori, et al., The glymphatic system: Current understanding and modeling, *IScience* 25 (9) (2022) 104987.
- [83] K. E. Holter, B. Kehlet, A. Devor, T. J. Sejnowski, A. M. Dale, S. W. Omholt, O. P. Ottersen, E. A. Nagelhus, K.-A. Mardal, K. H. Pettersen, Interstitial solute transport in 3D reconstructed neuropil occurs by diffusion rather than bulk flow, *Proc. Natl. Acad. Sci.* 114 (37) (2017) 9894–9899.
- [84] V. Vinje, G. Ringstad, E. K. Lindstrøm, L. M. Valnes, M. E. Rognes, P. K. Eide, K.-A. Mardal, Respiratory influence on cerebrospinal fluid flow—a computational study based on long-term intracranial pressure measurements, *Sci. Rep.* 9 (1) (2019) 9732.
- [85] C. Daversin-Catty, V. Vinje, K.-A. Mardal, M. E. Rognes, The mechanisms behind perivascular fluid flow, *Plos one* 15 (12) (2020) e0244442.
- [86] M. Croci, V. Vinje, M. E. Rognes, Uncertainty quantification of parenchymal tracer distribution using random diffusion and convective velocity fields, *Fluids Barriers CNS* 16 (1) (2019) 32.
- [87] Z. Rajna, L. Raitamaa, T. Tuovinen, J. Heikkilä, V. Kiviniemi, T. Seppänen, 3D multi-resolution optical flow analysis of cardiovascular pulse propagation in human brain, *IEEE Trans. Med. Imaging* 38 (9) (2019) 2028–2036.

- [88] M. Hornkjøl, Mhornkjol/mri2fem-ii-chapter-3-code: Full release, Zenodo (2024).
- [89] P. E. Goa, S. Blömer, R. Stirnberg, T. Stöcker, Brain pulsation imaging using non-balanced steady-state free precession with 3D-EPI readout, *Magn. Reson. Med.* (2025).
- [90] S. M. Ulv Larsen, S. C. Holst, A. S. Olsen, B. Ozenne, D. B. Zilstorff, K. Brendstrup-Brix, P. Weikop, S. Pleinert, V. Kiviniemi, P. J. Jennum, et al., Sleep deprivation and sleep intensity exert distinct effects on cerebral vasomotion and brain pulsations driven by the respiratory and cardiac cycles, *PLoS Biol.* 23 (11) (2025) e3003500.
- [91] L. Ray, J. J. Iliff, J. J. Heys, Analysis of convective and diffusive transport in the brain interstitium, *Fluids Barriers CNS* 16 (1) (2019) 6.
- [92] V. Vinje, B. Zapf, G. Ringstad, P. K. Eide, M. E. Rognes, K.-A. Mardal, Human brain solute transport quantified by glymphatic MRI-informed biophysics during sleep and sleep deprivation, *Fluids Barriers CNS* 20 (1) (2023) 62.
- [93] C. Burstedde, L. C. Wilcox, O. Ghattas, P4est: Scalable algorithms for parallel adaptive mesh refinement on forests of octrees, *SIAM J. Sci. Comput.* 33 (3) (2011) 1103–1133.
- [94] W. M. Boon, M. Hornkjøl, M. Kuchta, K.-A. Mardal, R. Ruiz-Baier, Parameter-robust methods for the Biot–Stokes interfacial coupling without Lagrange multipliers, *Journal of Computational Physics* 467 (2022) 111464.
- [95] J. J. Lee, E. Piersanti, K.-A. Mardal, M. E. Rognes, A mixed finite element method for nearly incompressible multiple-network poroelasticity, *SIAM J. Sci. Comput.* 41 (2) (2019) A722–A747.
- [96] K.-A. Mardal, M. E. Rognes, T. B. Thompson, L. M. Valnes, *Mathematical modeling of the human brain: from magnetic resonance images to finite element simulation*, Springer Nature, 2022.
- [97] J. S. Dokken, K.-A. Mardal, M. E. Rognes, , L. M. Valnes, V. Vinje, *Mathematical Modelling of the Human Brain II – From Glymphatics to Deep Learning*, Springer Nature, 2025.